2013

Photocurrent, Photoluminescence and Exciton Dynamics in Rubrene Molecular Single Crystals

ByungGook Lyu
Lehigh University

Recommended Citation

Lyu, ByungGook, "Photocurrent, Photoluminescence and Exciton Dynamics in Rubrene Molecular Single Crystals" (2013). *Theses and Dissertations.* Paper 1550.

Photocurrent, Photoluminescence and Exciton Dynamics in Rubrene Molecular Single Crystals

by

ByungGook Lyu

A Dissertation
Presented to the Graduate Committee
of Lehigh University
in Candidacy for the Degree of
Doctor of Philosophy
in
Physics

Lehigh University
September 2013

Approved and recommended for acceptance as a dissertation in partial fulfillment of the requirements for the degree of Doctor of Philosophy.

ByungGook Lyu
Photocurrent, Photoluminescence and Exciton Dynamics in Rubrene Molecular Single Crystals

Date

Ivan Biaggio, Dissertation Director, Chair

Accepted Date

Committee Members

Volkmar Dierolf

W. Beall Fowler

Michael J. Stavola

Himanshu Jain

Acknowledgements

First of all, I would like to thank my advisor, Professor Ivan Biaggio, who has helped a struggling student to the end. He has shown incredible excellence and intelligence, fulfilling and supporting me all the way.

Second, I want to thank my committee members, Professors Volkmar Dierolf, Fowler, Stavola, Jain, for all the extra help that allowed me to finish my degree.

And, of course, I thank our collaborators, my research group, friends. Everyone was supportive during my grad school.

Special Thanks to Professor Kim and my parents, they have looked over me all my life. Thanks also to Son-Hee, Jerome, Desmond, Dominic, and Alina for all your encouragements.

Contents

List of Figures

Abstract

This work discusses the photocurrent and photoluminescence that can be induced by short-pulse illumination in rubrene single crystals. The pulsed illumination excites a rubrene molecule from the ground state to its first optically accessible excited state, resulting in a singlet exciton state. In rubrene, a singlet exciton can transform into two triplet excitons which together have a spin of zero by an efficient spin-conserved *fission* process. On the other hand, two triplet excitons can interact to again form a singlet exciton by a *fusion* process. Quantitative modeling of the transformation of singlet excitons into triplet excitons and vice-versa shows that both photoconductivity dynamics and photocurrent dynamics after pulsed excitations can be understood within the same framework.

The photoluminescence observed after pulsed excitation is only emitted upon radiative recombination of singlet excitons. A simple model of fission and fusion based on rate equations leads to a qualitatively different photoluminescence dynamics depending on the time scale. In particular, it predicts a fast exponential decay corresponding to the initial fission process, later a power-law (quadratic) decay corresponding to a regime when triplet-triplet interaction is dominant, and a

final exponential decay with a time-constant which is half the triplet exciton lifetime. This last exponential decay corresponds to the case when only a lower density of triplet excitons is left.

The same model can be used to predict the photocurrent dynamics after pulsed excitation. Experimental observations after pulsed illumination show that, for low excitation pulse energies, a large photocurrent grows exponentially with a time constant of the order of $\sim$ 100 μs. This photocurrent build-up time then becomes shorter at higher excitation energies, with the peak photocurrent also saturating. One finds that the observed photocurrent dynamics can be reproduced with the same model based on exciton fission and fusion that successfully explained photoluminescence dynamics. The only additional assumption that is required to do so is that triplet excitons be able dissociate and release free holes by direct interaction with a defect state. The 100 μs build-up time of the impulsively induced photocurrent then corresponds to the triplet lifetime.

Chapter 1

Introduction

1.1 Organic Molecular Crystals

This work will focus on organic molecular crystals that consist of of an ordered assembly of organic molecules held together by Van der Waals forces. In many cases, some properties of such crystals can be predicted by treating them as an "oriented molecular gas." The energy can be localized in a single molecule during its lifetime in the excited state. In order to understand the electronic structure of molecular crystals, one has to also take into account the interaction between the molecules. Specifically, the interaction between an excited molecule and its unexcited neighbors. However, this interaction is weak in organic crystals, which are bound by weak Van der Waals forces, and one typically observes low charge carrier mobilities, of the order of (1 cm^2/Vs). From the macroscopic point of view, such crystals have relatively low melting and sublimation temperatures, and low mechanical strength. Simple growth procedures and stability at room temperatures for many organic molecular crystals make them good candidates for applications such as organic FET (Field Effect Transistors) [1–4]. A fundamental energy state in such systems, an exciton (an electron bound to a hole), typically has lifetimes on the order of picoseconds to nanoseconds, which in some extreme cases can go up to milliseconds or even more. As can be observed with any excited state, excitons can also demonstrate various behaviors such as propagation through the crystal lattice, interacting with other molecules, traps and other excitons [5]. The weak nature of the Van der Waals force that binds molecules together in a molecular crystal creates a strong tendency of charge carrier and exciton localization [5, 6].

1.1.1 Excitons in Organic Molecular Crystals

Excitons in molecular crystals, characterized by their lifetime and diffusivity, can also contribute to charge carrier creation [5, 6]. In many cases, excitons are created by a direct photoexcitation, or from charge carrier relaxation. This work focuses on directly photoexcited excitons, which allows a direct control over the exciton spatial distribution and population density. Because exciton decay contributes to the observable luminescence and charge carrier creation, the two main physical observables are excitonic luminescence and photocurrent, both resolved in time.

1.2 Rubrene molecule and rubrene single crystal

Rubrene (5,6,11,12 - tetraphenylnaphthacene) belongs to the group of polycyclic aromatic hydrocarbons and is well known as a sensitizer in chemiluminescence. The rubrene molecule consists of four benzene rings (the molecular backbone is equal to tetracene) and four substituted phenyl groups attached to the two internal rings. The rubrene molecule as it is found in orthorhombic rubrene single crystals [7] is centrosymmetric with a twofold axis of rotation along the short backbone (Fig. 1.1). Vapor transport [8] grown rubrene crystals are orthorhombic [7], with four molecules per unit cell. The lattice constants are $a = 14.4$ Å, $b = 7.18$ Å, and $c = 26.9$ Å.

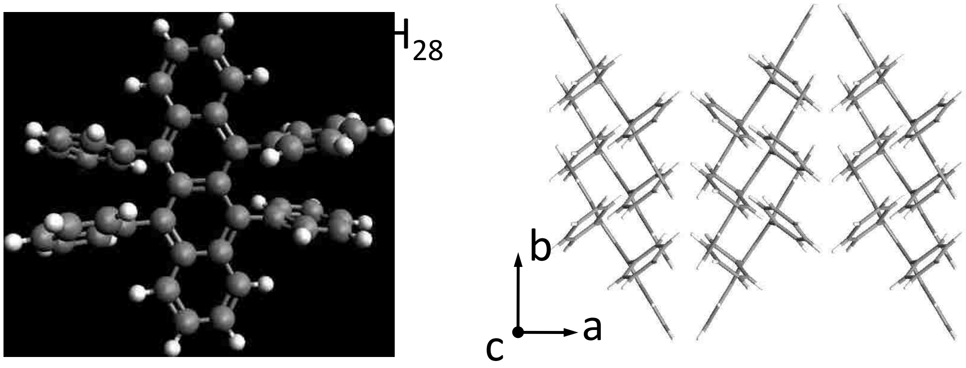

Figure 1.1: Structure of a rubrene molecule (left), molecular packing in the ab-plane (right).

A theoretical model characterizing triplet fusion is expanded in this work to explain the experimentally measured extraordinary photocurrent and photoluminescence dynamics in rubrene single crystals. Chapter 2 discusses an extension of the model to explain exciton dynamics. The luminescence dynamics is modeled based on various initial conditions. In Chapter 3, a numerical simulation of an electric field in the sample is performed to check for corrections in photocurrent measurements. In Chapter 4, this model is extended to address various characteristics of photocurrent. Chapter 5 reviews several recent experiments in rubrene where photoluminescence and photocurrent dynamics have been observed, and discusses how these observations can be interpreted with the physical picture discussed in chapter 4. Finally, Chapter 6 presents a summary, addresses global conclusions, and proposes future research directions.

Chapter 2

Exciton Dynamics in Molecular Crystals

2.1 Introduction and background

In rubrene, both absorption and photoluminescence spectra are in the visible spectral range, and common laser light sources and detection tools such as spectrometers and photomultiplier tubes can be conveniently used. Since photoluminescence (PL) can be easily measured experimentally, it can be used as a probe to study the dynamics of photoexcited states in a material. In general, absorption of a photon in this class of materials typically leads to a creation of an exciton or of a charge carrier pair, depending on the conditions of excitation. In rubrene, in most cases, absorption of a photon results in creation of a singlet exciton with zero total angular momentum. The lifetime of this singlet exciton, extracted from a temporal exponential decay of the photoluminescence signal, was found to be 15 ns [9] for rubrene

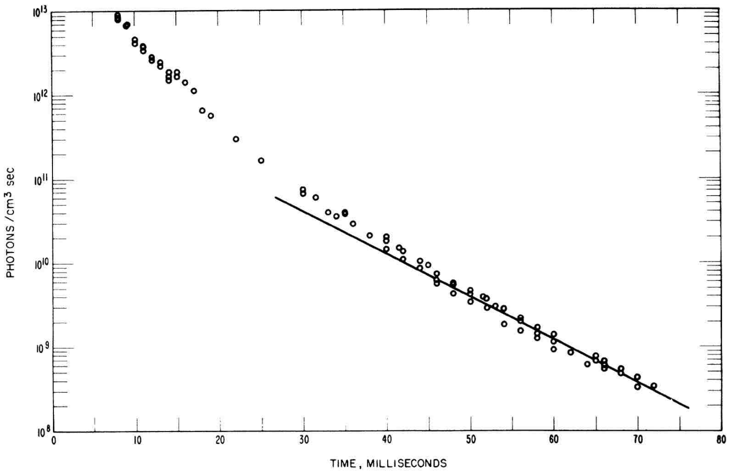

Figure 2.1: Semilog plot of fluorescence power versus time, as measured in Anthracene (From Ref. [10]).

molecules measured in solutions. On the other hand, a similar measurement in a rubrene single crystal gives a more complex time dynamics of the photoluminescence. In the nanosecond regime, the photoluminescence is characterized by an exponential decay with a decay constant of few nanoseconds. On the longer time scales, photoluminescence dynamics is sometimes governed by a quadratic decay, which becomes an exponential decay again (but with a different decay constant). A detailed discussion of this complicated behavior is presented in this chapter.

2.1.1 Photoluminescence dynamics in anthracene

Early measurements in anthracene have also revealed an existence of a long-lived luminescence [10–12]. Instead of a typical exponential temporal decay of the PL signal normally observed, a more complicated time dynamics behavior was observed [13].

Observed PL dynamics in anthracene in Figure 2.1 show two interesting features. First, a large overall lifetime of the PL indicate a long-lived energy state, which was assigned to long-lived triplet excitons. Triplets are composed of a bound electron and a hole of the same spin, which results in a non-zero net angular momentum. While direct decay to the ground state is allowed for singlets, for triplets direct relaxation to the ground state is forbidden by selection rules, which results in much longer triplet lifetimes, often of the order of milliseconds, of even longer. Singlets typically decay within nanoseconds. Second, because excitons are characterized by their natural lifetimes, the decay of the corresponding populations would still lead to an observed exponential decay of the luminescence signal. The PL dynamics on anthracene, on the other hand, showed a quadratic dependence on time. A new model was constructed that would include interaction between excited states to explain the behavior observed from the experiment. A quadratic dependence can be associated with a fusion process of energy levels, for which the rate of interaction is dependent on the population density. Additionally, triplets were identified as this energy state undergoing fusion, when considering its extra long lifetime to be observable in the millisecond regime. If triplets were to interact with each other to create singlets, the decay would be number-density-dependent, and, in this particular case, would decay quadratically. In later experiments performed with rubrene single crystals, the existence of triplets was also observed, and was shown to play a large role in the exciton dynamics [14]. A model that can be used to rationalize such exciton dynamics, like the one observed in rubrene single crystals, will be discussed next.

2.2 Modeling of exciton dynamics

We start with a population of singlet excitons directly photoexcited by a short laser pulse, giving a well-defined number of excited states at time zero. A fraction of the directly created singlet excitons can then rapidly decay with a lifetime of the order of a few nanoseconds or less. Simultaneously, singlet excitons also have a probability to convert into triplet states via well-known processes such as intersystem crossing, or the spin-conserved singlet fission [15–19]. In order to explain the observed quadratic decay of the luminescence, we consider the possibility of triplet-triplet interactions that can recreate singlet excitons, which will then again have a probability to decay radiatively. The processes of exciton fission and fusion can only be efficient when singlet energy is nearly equal to twice the triplet energy [20], where fission is efficient if the triplet energy is less than half of a singlet, and fusion is efficient if the triplet energy is more than half of a singlet. Triplet exciton fusion in this case creates a single singlet exciton from a pair of triplets states. The existences of both efficient singlet fission and triplet fusion in rubrene have been observed. The time evolution of the singlet and triplet population densities in the presence of fission and fusion processes can be described mathematically by the following rate equations:

$$\frac{ds}{dt} = -\delta s - \frac{s}{\kappa} + \frac{1}{2} n_s \gamma p^2 - ls \tag{2.1}$$

$$\frac{dp}{dt} = -\gamma p^2 - \frac{p}{\tau_p} + 2\delta s \tag{2.2}$$

Here, p is the population density of triplet excitons, γ is the rate at which triplet excitons interact with each other, thus the corresponding term in the equation contains the population density of triplets squared. τ_p is the lifetime of a triplet exciton, and s is the population of singlet excitons. δ is the rate at which singlet excitons create triplet excitons. A factor of 2 indicates that two triplets are created by a single singlet. κ is the non-radiative lifetime of a singlet exciton, which could be related to charge carrier creation. The term ls is a radiative decay term. The $n_s\gamma p^2$ term corresponds to the singlet excitons that are created by triplet exciton fusion, where n_s is the rate of singlets to be created by the triplets, and $1/2$ is also multiplied to this term since two triplets will create one singlet. This finite probability takes into account the fact that not all triplet collisions will result in a singlet creation. The rate equations presented above are constructed to be as general as possible, and include all possible mechanisms for singlet and triplets exciton creation and destruction. However, from a practical point of view, it is convenient to distinguish the terms related to the physical observables (photoluminescence) , and to combine all the remaining terms. Then, the equations above can be simplified to

$$\frac{ds}{dt} = +\frac{1}{2}n_s\gamma p^2 - \frac{s}{\tau_s}, \tag{2.3}$$

$$\frac{dp}{dt} = -\gamma p^2 - \frac{p}{\tau_p} + n_p\frac{s}{\tau_s} \tag{2.4}$$

and τ_s is the lifetime of singlet excitons,

$$\frac{1}{\tau_s} = \delta + l + \frac{1}{\kappa} \tag{2.5}$$

Further, the probability for triplets to be created by the singlets via fission is

$$n_p = \frac{2\delta}{\delta + l + \frac{1}{\kappa}}, \tag{2.6}$$

The factor 2 here takes into account that two triplets are created from a single singlet.

2.3 Time evolution of the singlet and triplet exciton populations

To address how the population of the excitons changes with time, we can take into account that triplet excitons have a much longer lifetime then singlet excitons, due to the fact that direct triplet decay to the ground state is forbidden. After a fast creation of singlet excitons via a short laser pulse, the singlet population will be mostly depleted within nanoseconds, and from that point in time mainly triplets will remain. This allows a convenient separation of the time scales at which singlets and triplets exist, and the triplet evolution can be treated starting at the point in time when the majority of singlets have undergone fission into a population of triplets, as given by the rate equations 4.7 and 2.2. The decay of the population of singlet excitons is directly related to the experimentally observed photoluminescence signal, hence the importance of the singlet population should not be underestimated. The evolution of the exciton populations undergo three distinct stages, as shown in the next Figure 2.2.

In Figure 2.2, a photoexcitation with a short laser pulse created an initial population of singlets with a population density of $s_0 = 10^{11}\ excitons/\mu m^3$. Each region

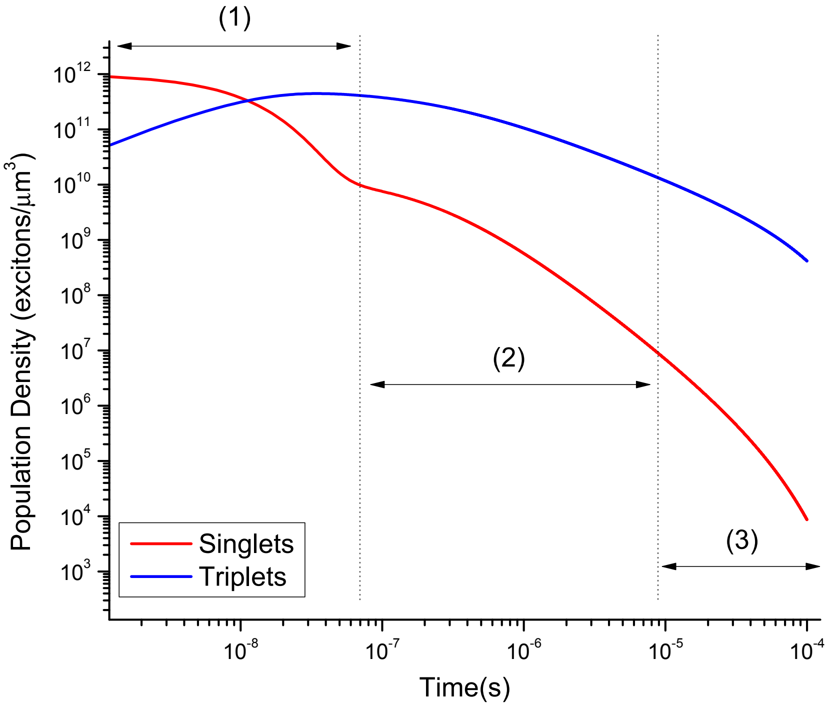

Figure 2.2: Evolution of the singlet and triplet exciton populations modeled using Eq.2.16 with $\tau_s = 10$ ns, $\tau_t = 50$ μs, $n_s = 1$, $n_p = 0.5$, $\gamma = 10^{-5}$, $s_0 = 10^9$ $excitons/\mu m^3$, $t_0 = 0$. Three distinct regions in the respective dynamics can be seen.

on Figure 2.2 has some distinct characteristics. We choose a log-log scale here to highlight certain distinct functional dependencies. Region 1 corresponds to first few nanoseconds after a population of singlets is created. It is characterized by a monoexponential decrease of the singlet density with a characteristic effective lifetime, and a simultaneous increase in the number of triplets created via singlet fission. The key feature in Region 2 is the power-law decay of both populations, with quadratic decay of singlets (resulting in the slope of -2 on a log-log plot), and with triplet density decaying like t^{-1} (hence a slope of -1 on the graph). Region 3 corresponds to even later times, where the triplet lifetime dominates the decay dynamics, and the corresponding decay dynamics becomes exponential again. Also, as singlet population depends on the triplet population squared, its decay also shows an exponential shape.

2.3.1 First few nanoseconds

In our model conditions, at time zero, a fast impulsive photoexcitation creates a well-defined population of singlet excitons that typically have a lifetime of the order of a few nanoseconds. During this lifetime, singlets radiatively decay and undergo fission to create long-lived triplet excitons. Excluding any possible triplet density contribution to creation of singlets in the first few nanoseconds, the rate equation for the singlet population becomes

$$\frac{ds}{dt} \approx -\frac{s}{\tau_s}, \tag{2.7}$$

with a simple solution

$$s(t) = s_0 e^{-\frac{t}{\tau_s}} \tag{2.8}$$

Detected luminescence, being proportional to the singlet density, will decay exponentially. On the other hand, the initial (first few nanoseconds) increase in the population of triplets is roughly given by the total number of singlets present. Due to the fact that the triplet creation by singlets is dominant at this time scale, the rate equation for the triplet population can be approximated as

$$\frac{dp}{dt} \approx +n_p \frac{s}{\tau_s} \tag{2.9}$$

which has a solution

$$p(t) = n_p s_0 (1 - e^{-\tau_s t}) \tag{2.10}$$

Regardless of fusion of triplets, one would still observe an exponential decay of singlets in this initial regime. Most observations [21, 22] are focused on this regime, making it difficult to detect additional properties and interactions of excitons such as triplet fusion.

2.3.2 Excitons in the microsecond time scale

After a few nanoseconds, the singlet population will be mostly depleted, and the dominant population is triplets. When the triplet population is large, the probability of the interaction between triplets is high and depends on the triplet density, thus the quadratic term in the rate equation 4.7 and 2.2 becomes dominant. The triplet rate equation is then

$$\frac{dp}{dt} \approx -\gamma p^2 \tag{2.11}$$

with a solution

$$p(t) = \frac{1}{\gamma t + \frac{1}{p_0}} \tag{2.12}$$

As previously discussed, the triplet-triplet interactions can re-create singlets via fusion. Newly created singlets also have a probability to either radiatively decay, or undergo fission again. Rate equation for the time scale for singlet population in equilibrium becomes

$$0 = \frac{ds}{dt} = +\frac{1}{2} n_s \gamma p^2 - \frac{s}{\tau_s} \tag{2.13}$$

which provides an important relationship

$$s = \frac{1}{2} \tau_s n_s \gamma p^2 \tag{2.14}$$

Although the population of singlets at this time scale is small, it is very important practically speaking, because the PL that originates from decaying singlets is the common convenient physical observable. Considering Eq 2.5, the luminescence created by the singlets is

$$\frac{1}{\delta + l + \frac{1}{\kappa}} l \frac{s}{\tau_s} = ls = \frac{1}{2} l \tau_s n_s \gamma p^2 \tag{2.15}$$

The luminescence power $L(t)$ emitted by singlets can further be expressed as

$$L(t) = \frac{1}{2} l \tau_s n_s \gamma \frac{1}{(\gamma t + \frac{1}{p_0})^2} \tag{2.16}$$

A simplified form of this equation can be obtained by taking $\gamma t >> 1/p_0$

$$L(t) = \frac{1}{2} l \tau_s n_s \gamma t^{-2} \tag{2.17}$$

which predicts that in this time scale, the observed photoluminescence power decays quadratically with time. A condition we have used is $\gamma t >> 1/p_0$. It indicates that with some appropriate time, photoluminescence will be independent of its initial population density, and will converge to a specific decay. This tendency will be revisited later.

It is important to keep in mind that the luminescence power defined here originates from a unit volume that has a certain population density of excitons.

2.3.3 Exciton dynamics at the millisecond time scale

Much later in time, we come to a point where the population densities of excitons are reduced strongly enough to make any interactions between individual excitons negligible, and the dynamics is governed by the triplet exciton lifetime. The rate equations that describe the system at these later times are

$$\frac{dp}{dt} = -\frac{p}{\tau_p} \tag{2.18}$$

with a solution being a simple exponential decay

$$p(t) = p_1 e^{-\frac{t}{\tau_p}} \tag{2.19}$$

where p_1 is triplet population density at some arbitrary time $t = 0$. While at these densities the quadratic term is insignificant for the triplet density dynamics, it still defines the rate at which detectable singlets are created. While the triplet population is given by Eq 2.19, we can use Eq 2.14 to obtain

$$s = \tau_s n_s \gamma p^2 = \tau_s n_s \gamma p_1^2 e^{-\frac{2t}{\tau_p}} \tag{2.20}$$

with corresponding PL power given by

$$L(t) = l {\tau_s}^2 n_s \gamma {p_1}^2 e^{-\frac{2t}{\tau_p}}, \tag{2.21}$$

a monoexponential decay with a time constant of a half of the triplet exciton lifetime τ_p.

2.3.4 Full solution in the microsecond and the millisecond regime

In most cases, singlet lifetime is dramatically smaller than that of a triplet. As was shown previously, at some point in time, typically after a few nanoseconds after photoexcitation, triplet population becomes much larger then singlet population. This allows to simplify Eq 2.2 (by assuming s = 0) and obtain a solution [23]

$$p(t) = \frac{p_0}{(1 + p_0\gamma\tau_p)e^{t/\tau_p} - p_0\gamma\tau_p} \tag{2.22}$$

which can be further approximated by considering the first two Taylor expanded terms (in the μs regime, t/τ_p is small) with respect to t,

$$p(t) = \frac{p_0}{(1 + p_0\gamma\tau_p)(1 + t/\tau_p) - p_0\gamma\tau_p} = \frac{p_0}{1 + (p_0\gamma + 1/\tau_p)t} \tag{2.23}$$

Next, we can ignore the $1/\tau_p$ term to arrive at

$$p(t) = \frac{1}{\gamma t + \frac{1}{p_0}} \tag{2.24}$$

which is the result we obtained before at Eq 2.12. In the millisecond regime, when the exponential term in Eq 2.22 becomes significantly larger then $p_0\gamma\tau_p$, Eq. 2.22 can be written as

$$p(t) = \frac{p_0}{1 + p_0\gamma\tau_p} e^{-t/\tau_p} \tag{2.25}$$

which again returns the exponential form for the millisecond regime similar to what was achieved at Eq 2.19. It is to be noted, for Eq 2.19 no quadratic decay in the microsecond regime was considered, unlike Eq 2.25 where this was considered. This explains the difference in the prefactor.

2.4 Numerical simulation of the photoluminescence dynamics

We have previously shown that the luminescence decay at the nanosecond (right after impulsive excitation) and the millisecond time scale have the shape of an exponential. For the nanosecond region, the PL curve is expected to scale linearly with the excitation pulse energy. Because the microsecond dynamics has a more complicated character, we want to examine its dependence on initial excitation conditions, such as excitation pulse energy and excitation wavelength. It is important to note that the wavelength of excitation light affects the spatial distribution of the created excitons, because of the wavelength-dependent absorption coefficient of the material. Therefore, two laser light pulses of the same total energy but different wavelengths result in different total densities of excitons that are distributed differently over the depth of the sample, which should be taken into account.

The following Figures is calculated using Eq 2.2 with the Runge-Kutta 4th method. The Runge-Kutta method is basically an extended Euler method; since

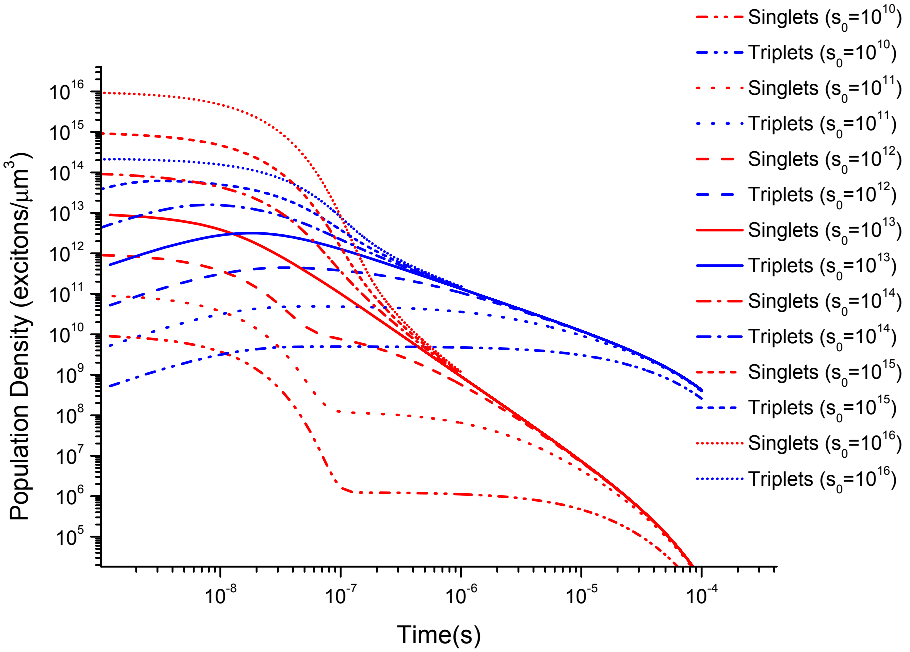

Figure 2.3: Modeling of the exciton dynamics after an impulsive excitation with different initial densities of singlet excitons. Curves are obtained using Eq 2.16 with $\tau_s = 10$ ns, $\tau_t = 50\ \mu s$, $n_s = 1$, $n_p = 0.5$, $\gamma = 10^{-5}$, $t_0 = 0$. The initial singlet population changes between $s_0 = 10^9$ and $s_0 = 10^{13}\ excitons/\mu m^3$.

the original Euler method have larger errors and have numerical instabilities, we extend trial steps on each interval to increase accuracy and stability. The fourth order is most common for its balance between low error and computational requirements in calculating ordinary differential equations. With a total of 9000 intervals, we start with an initial singlet population density and no triplet population density at 1 ns and proceed to 100μs. The log-log plot is used to highlight certain functional dependencies, and for convenient comparison of different time scales.

Several interesting features can be readily seen on Fig 2.3. The first straightforward observation is the nearly linear relationship between the total amount of generated triplets and the initial density of singlets, as expected. Secondly, one can notice a characteristic transition point at around $100ns$ in the singlet decay curve from exponential to quadratic decay. The occurrence of this transition in time strongly depends on the initial singlet population. In other words, it corresponds to the time point where the relative significance of the initial population of singlets decaying exponentially becomes less than the delayed contribution of singlets due to triplet fusion. As a consequence, for high initial singlet densities, the majority of the integrated photoluminescence occurs on the microsecond scale and originates from singlets re-created via fusion. In general, under a weak fission of singlets to triplets and/or a weak fusion, the efficiency of microsecond scale luminescence dramatically drops.

Another notable feature is predicted in the approximation Eq 2.17. As seen in Figure 2.3, regardless of initial population density, the singlet and triplet populations have a tendency to merge into the same decay. In Eq 2.17, it was predicted that after some time, the photoluminescence will decay quadratically into the same form, regardless of population density.

2.4.1 Effect of triplet-triplet interaction efficiency on the exciton population decay dynamics

In general, various external factors such as temperature, etc. may have a strong effect on the triplet interaction rate γ, and subsequently on the dynamics of both singlet and triplet exciton population.

As can be seen in Figure 2.4, there is a strong influence on the amount of re-created singlets on the microsecond time scale and the value of γ. Further, for lower γ values one can see that the reduction of the triplet population due to fusion is

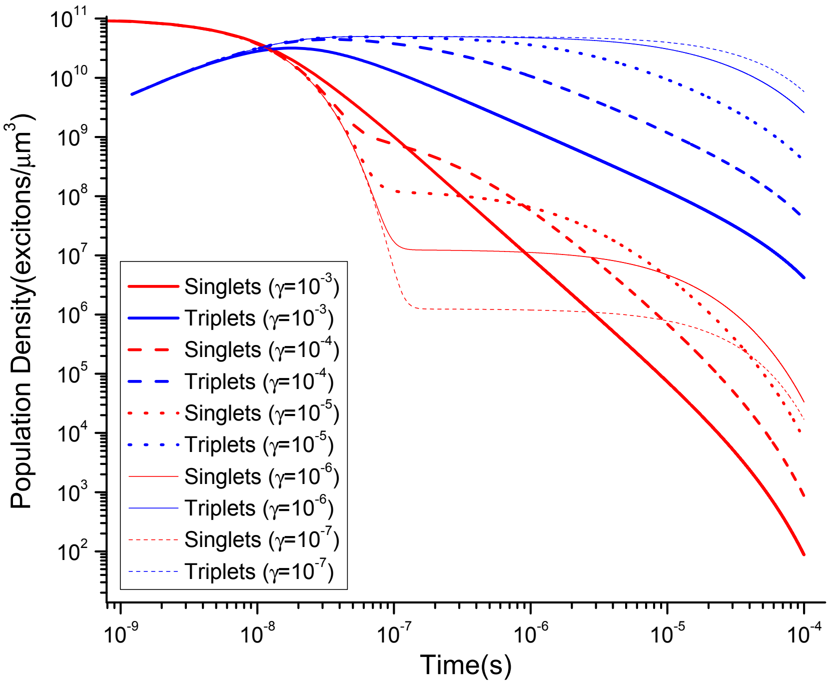

Figure 2.4: Exciton dynamics after impulsive excitation for different triplet-triplet interaction rates. Decay curves were generated using equation 2.16 with $\tau_s = 10ns$, $\tau_t = 50\mu s$ $n_s = 1$, $n_p = 0.5$, $s_0 = 10^{11}$, $t_0 = 0$. The triplet-triplet interaction rate γ was varied between 10^{-3} and 10^{-7} $excitons/\mu m^3$.

minimal, and the effect of triplet lifetime becomes more significant.

2.4.2 Exciton decay dynamics with different triplet lifetimes

Triplet lifetime can be varied by, for example, an introduction of traps in the system that might intercept triplets to create charge carriers. This possibility will be further discussed in Chapter 4. In Figure 2.5 we model how the variations in the τ_t affect the exciton population dynamics.

As expected, for longer triplet lifetimes the shape of the triplet decay curves

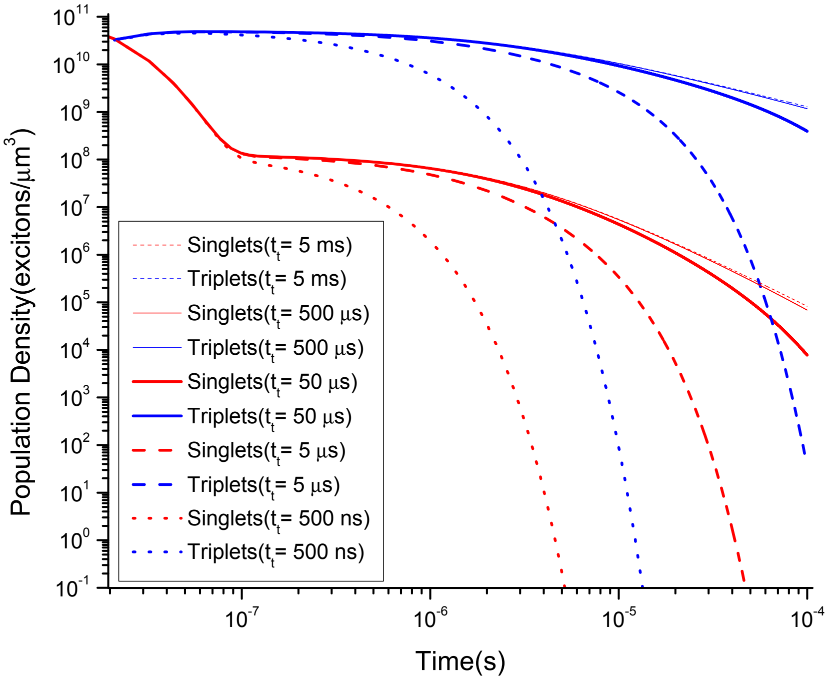

Figure 2.5: Exciton dynamics after impulsive excitation corresponding to various triplet exciton lifetimes. Decay dynamics was modeled using Equation 2.16 with $\tau_s = 10ns$, $\gamma = 10^{-5}$, $n_s = 1$, $n_p = 0.5$, $s_0 = 10^{11}\ excitons/\mu m^3$, $t_0 = 0$. Curves correspond to triplet lifetime values $\tau_t = 500ns, 5\mu s, 50\mu s, 500\mu s$, and 5 ms.

is dominated by the fusion process. When τ_t becomes significantly small, however, triplet lifetime starts to compete with the triplet population decay via fusion. Further, for shorter triplet lifetime values, the triplet lifetime dynamics dominate any effect by the singlet generation via fusion, and a quadratic decay previously predicted in the microsecond region transforms into an exponential decay.

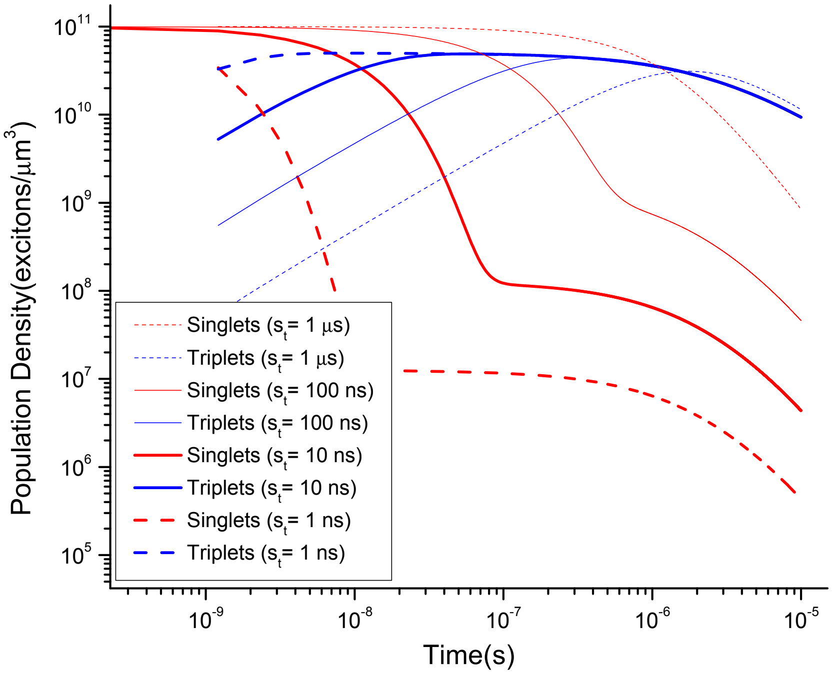

Figure 2.6: Exciton dynamics after impulsive excitation with different modeled using various singlet exciton lifetimes. Equation 2.16 was used with $\tau_t = 50\mu s$, $\gamma = 10^{-5}$, $n_s = 1$, $n_p = 0.5$, $s_0 = 10^{11}$, $t_0 = 0$. Singlet lifetimes were changed between τ_s= 1 ns and 1 μs.

2.4.3 Exciton population decay dynamics with various singlet exciton lifetimes

Here we explore the effect of the singlet exciton lifetime on the exciton decay dynamics. This does not alter the probabilities for individual radiative vs non-radiative vs fission to triplets, but the overall lifetime of singlets.

The main feature in Figure 2.6 is that a reduction in the singlet lifetime results in a more rapid increase in the triplet population. This further results in a lower amount of singlets found in the microsecond region, as predicted by Eq. 2.14. If τ_s is made significantly large, the maximum of the triplet population occurs much later, but in all cases it reaches a similar maximum value, but with considerably different amount of remaining singlets in the same time region. This behavior is also expected from Eq. 2.14, that predicts the singlet population to be proportional to the singlet lifetime τ_s.

2.4.4 Exciton decay dynamics with a constant number of photons in the excitation pulse

As stated, the theory relies heavily on the exciton population density. Since the exciton population density is dependent on the absorption constant for the wavelength of the excitation light, we can investigate a fixed population of excitons, where only the distribution changes by the absorption. A wavelength dependent experiment can be executed in this fashion, by maintaining a constant number of photons, as the absorption coefficients will determine the exciton population densities.

As seen in Figure 2.7, high exciton densities of $s_0 = 10^{13} excitons/\mu m^3$ introduce a fast supply of singlets decaying quadratically, whereas for low densities of $s_0 = 10^{10}$, the supply of singlets from triplet-triplet fusion is relatively weak. Since triplet "consumption" is weak, triplet decays are slower.

The results in this case of a constant total population with different densities are similar with the calculations of Figure 2.3. When we compare the exciton dynamics in the fixed population calculation (Figure 2.7) with different population density calculations (Figure 2.3), the exciton dynamics characteristics are similar. Even when the total number of excitons are fixed, one can resort to Figure 2.3 to recognize the differences in excitons dynamics by just normalizing the magnitude.

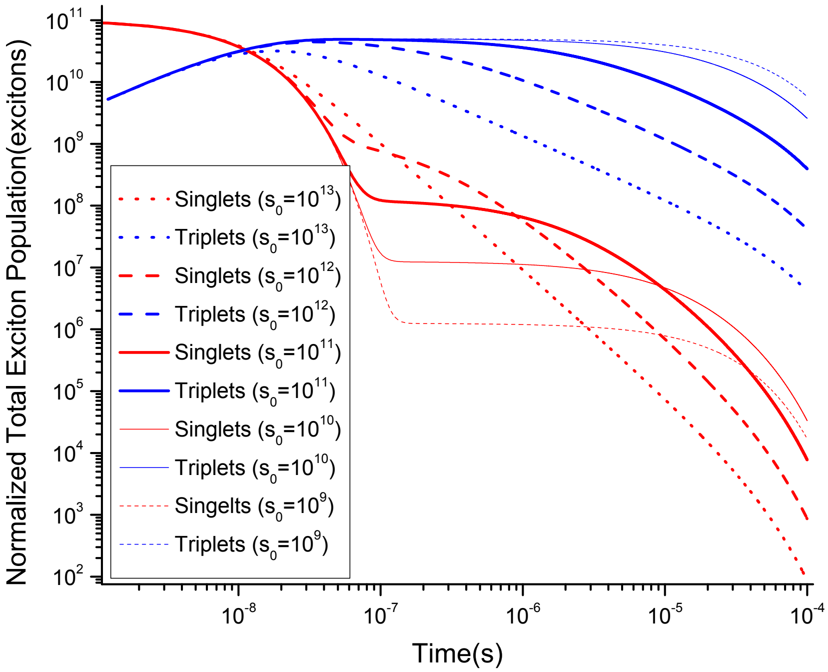

Figure 2.7: Exciton dynamics after impulsive excitation with a fixed total exciton population, and not population densities which were considered previously. Equation 2.16 was used with $\tau_s = 10ns$, $\tau_t = 50\mu s$ $n_s = 1$, $n_p = 0.5$, $\gamma = 10^{-5}$, $s_0 = 10^9, 10^{10}, 10^{11}, 10^{12}, 10^{13}$ $excitons/\mu m^3$, $t_0 = 0$, where the total volume is $1\mu m^3$

2.5 A case of non-homogeneous excitation density

For simplicity, up to this point, our modeling assumed homogeneous density of photoexcited excitons. In reality, in most cases, photoexcitation results in a distribution of excitons(singlets) where population density decays exponentially with depth. By considering multiple layers of photoexcited material, we correct for the fact of non-homogeneous excitation. One can argue that since exciton diffusion [15] is essential for triple-triplet fusion, one should take it into account and consider how the diffusion can correct the corresponding population densities. However, because diffusion

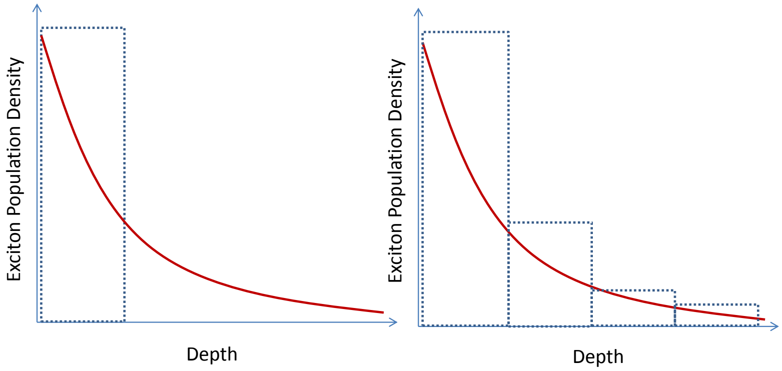

Figure 2.8: Distribution of excitons after an impulsive photoexcitation and its possible approximations. Previous calculations were performed with an approximation of a homogeneous exciton population density distribution (left). The right figure shows an improved density approximation that considers multiple layers of photoexcited material.

of triplets in rubrene single crystals was shown to be much smaller than the absorption length [24], and thus to have practically no effect on exciton distribution, we can safely ignore exciton diffusion.

Figure 2.8 shows two possible approximations that were used. A spatially homogeneous exciton population used for calculations above is shown on the left side. A refined approximation that considers multiple layers is on the right.

The calculations of the contribution of each layer is similar to the one done before in Figure 2.7. It can be seen in Fig. 2.9 that the refined result differs slightly, but its overall dynamics is very similar to the one with homogeneous approximation. Hence, a homogeneous layer approximation can be sufficient for rough exciton dynamics

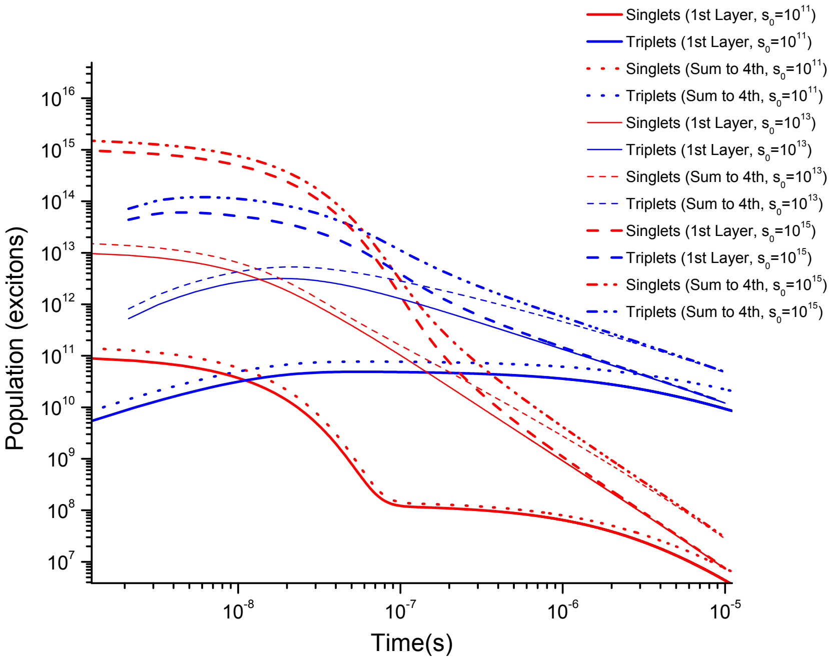

Figure 2.9: Modeling with multiple layers of different population density. Calculation was done using Eq. 2.16 with $\tau_s = 10ns$, $\tau_t = 50\mu s$, $\gamma = 10^{-5}$, $n_s = 1$, $n_p = 0.5$, $s_0 = 10^{11}\ excitons/\mu m^3$, $t_0 = 0$.

predictions.

This approximation can be understood easily by recognizing that most excitons are absorbed near the surface, so the density with the majority of excitons is bound to dominate the total exciton dynamics as well. Any additional layer will have only a fraction of the previous layer, and since the density does not change by orders of magnitudes (for it to have any significant exciton dynamics difference) but rather just a fraction, the additional layer will behave similarly to its previous layer.

There is one characteristic that varies; since the later layers do not consume triplets as fast as the first layer, they will have a more vivid representation in longer times such as at 10 μm seen in Figure 2.9. Although for $s_0 = 10^{11}$, 10 μs was not long enough to merge with other exciton dynamics, one can see that the first layer approximation will merge into a single dynamics curve, predicted by Eq. 2.17, and also the multi layer approximations also merge into a different dynamics curve.

2.6 Conclusion

In this chapter, we focused on exciton behavior of fission of singlets to triplets, and fusion of triplets to singlets. We have presented a model which explains the fusion and fission process, and achieved various approximations to predict the exciton dynamics characteristics, such as the existence of a long lived μs population of excitons. We have also calculated how the exciton dynamics will change with different population densities, different singlet and triplet lifetimes, and different interaction coefficients. We have also shown that applying a simple calculation is sufficient to recognize photoluminescence characteristics.

Chapter 3

Possible experimental configurations for photoconductivity measurements

An alternate method of detecting exciton behavior is through one of its easily detectable byproducts – charge carriers. By applying an electric field and detecting its photocurrent, one can detect creation and decay of charge carriers.

One of the difficulties encountered while analyzing photocurrent measurements data is that the electric field applied in the region of photoexcitation may not in general be homogeneous, which could lead to incorrect photocurrent data interpretation. Hence, below we will investigate the proper conditions that create a constant and well-defined electric field in the sample. With a certain potential difference applied and the dielectric constant known, the electric field distribution will depend purely on the configuration of the contacts applied on the surface of the sample.

When photoexcitation occurs on the surface of the sample, the absorption of photons and creation of excitons have an exponential distribution in the depth (hence mostly on the surface, and less in the bulk of the crystal). The charge carriers are directly created by excitons, so the distribution of excitons determines the distribution of charge carriers. Free charge carriers are detected with an electric field created by the contacts, and the electric field distribution can be non-homogeneous.

We had no confirmation that the change of electric field magnitude should be of consideration while interpreting photocurrent. If the electric field were to decay significantly compared to the absorption depth where the excitons are distributed, additional calculations are needed for long wavelength excitation induced photocurrent measurements.

To validate this possibility, we calculate the electric field by solving Poisson's Equation in configurations commonly used. We will check if any corrections are needed for the photocurrent measurements analysis, and will propose strategies for future photoexcitation experiments interpretations executed with different sample configurations.

With a 3D differential equation calculator(FlexPDE, Partial Differential Equations Calculator), we use Poisson's Equations $\nabla^2\varphi = 0$ to calculate the electric field distribution in the system from the boundary conditions imposed by the contacts. The dielectric constant of rubrene of 2.6 was used [25]. The sample configuration used in our calculation is 1 cm long, and 5 mm wide. One must note that, due to symmetry, there is no vertical electric field component at this coordinate, thus the electric field vector will be parallel to the surface.

A schematic of a rubrene sample is shown in Figure 3.1. The excitation would

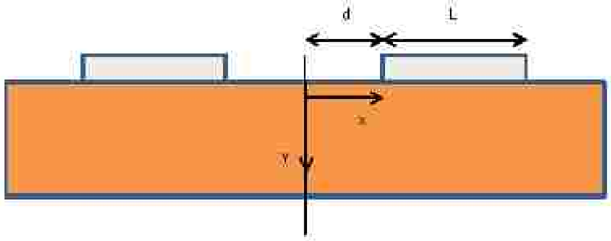

Figure 3.1: A cross-section of a rubrene sample is shown with variables defined. The dielectric constant for the sample is 2.6 [25], for the metal contact is 1e6, and for the surrounding air is 1. The potential difference between the contacts is 1 V. The thickness of the metallic contacts is 100 μm.

occur at the exact middle of the upper surface of the sample. Depending on the excitation wavelength, the excitons (and charge carriers) will be distributed along the vertical axis, defined as the y-axis in Figure 3.1. Two metallic contacts are positioned on top of the sample. Other sample configurations, such as samples with metallic contacts are above and below the sample in a “sandwich” configuration.

The following configurations were investigated. First, the distance between the contacts (defined as ’d’ in (1) of Figure 3.2) was increased. Second, rather than increasing the distance between the contacts, the contact were extended outwards in hope of homogenizing the electric field (by increasing ’L’ in (2) of Figure 3.2). Third, the electric field distribution for samples of different thickness were calculated (by increasing the thickness of the sample in the y-direction in (3) of Figure 3.2). Fourth, a sample was calculated where the contacts cover the whole surface except for a small “slit”, (which is equivalent to a very small ’d’ in (4) of Figure 3.3). Fifth, the electric field was calculated from a sample while moving away from a pair of contacts on the surface (shown in (5) of Figure 3.3). Sixth, contacts were applied

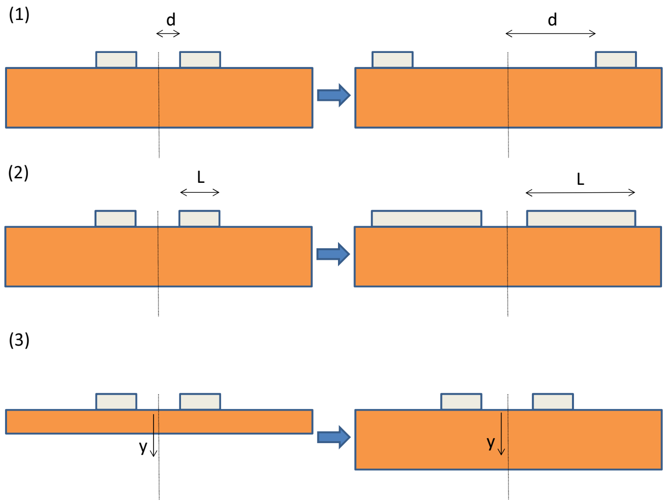

Figure 3.2: The electric field was calculated on the dotted line when (1) the distance between the contact varies, (2) the length of the metallic contacts are increased, (3) different thickness samples are used.

on the top and bottom of the sample to construct a “sandwich” configuration and the electric field distribution (shown in (6) of Figure 3.3) were measured.

3.1 Effect of the contact distance on the electric field distribution

The most commonly used sample configuration is shown in 3.1, where two contacts are positioned above the sample. The electric fields for various distances between the contacts is then calculated.

The configuration and electric potential distribution are shown in Figure 3.4 and the electric field for the increasing contact distance is shown in Figure 3.5. The

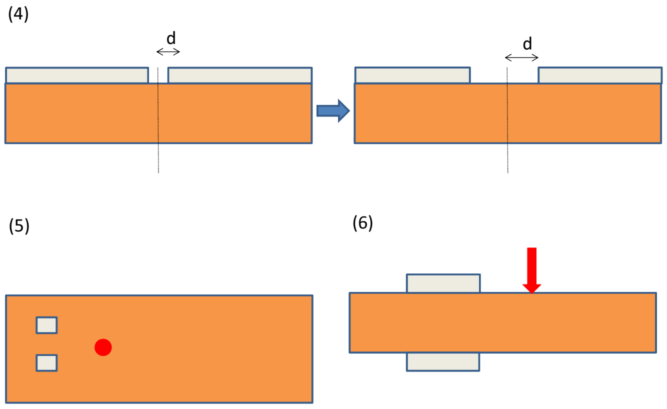

Figure 3.3: The electric field was calculated along the dotted line when (4) there was a small slit, (5) there was no excitation between the contacts but from a distance, (5) the contacts were a "sandwich" configuration.

surface of the sample is set to be at 0, and the sample ends at 0.3.

The decrease of the electric field with depth is rapid when the distance between the contacts are smaller then 1.4mm. When the distance between the contacts increases, a homogeneous electric field is created. As long as some distance exists one can create a rather reliable electric field for when the decay of electric field with depth is negligible.

Figure 3.5 also shows that even when the contacts are very close at 0.2mm distance, the change of electric field within $100\mu m$ where most of the excitation occurs, is minimal. We can safely conclude that photocurrent measurements on a typical rubrene sample of this configuration do not require much correction.

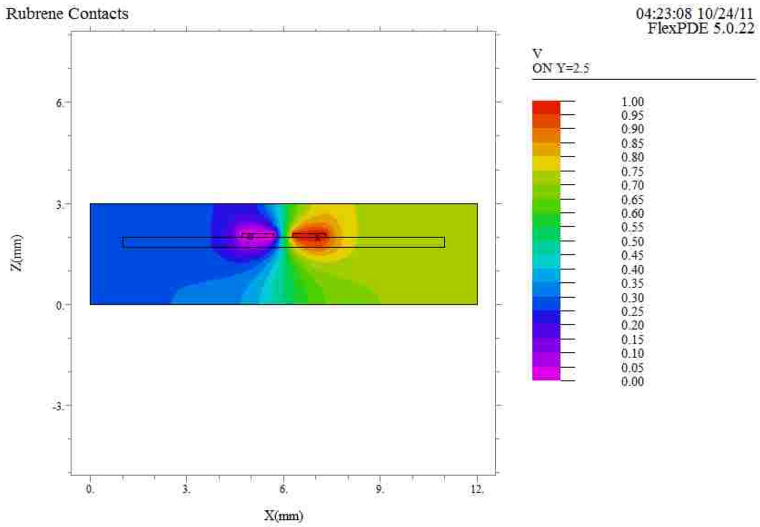

Figure 3.4: Potential distribution when contact distance changes. The rubrene sample has a thickness of 300 μm.

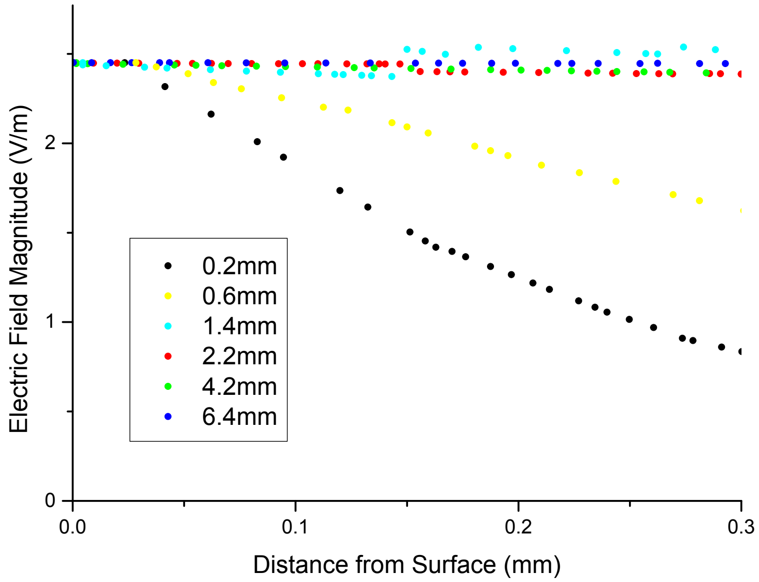

Figure 3.5: Effect of the contact distance on the field distribution.The dielectric constant for the sample is 2.6, for the metal contact is 1e6, and for the surrounding air is 1. The same electric field near the surface was maintained. The thickness of the contacts is 100 μm. The default sample thickness is 300 μm. The distance “d” are 0.2mm, 0.6mm, 1.4mm, 2.2mm, 4.2mm, and 6.2mm

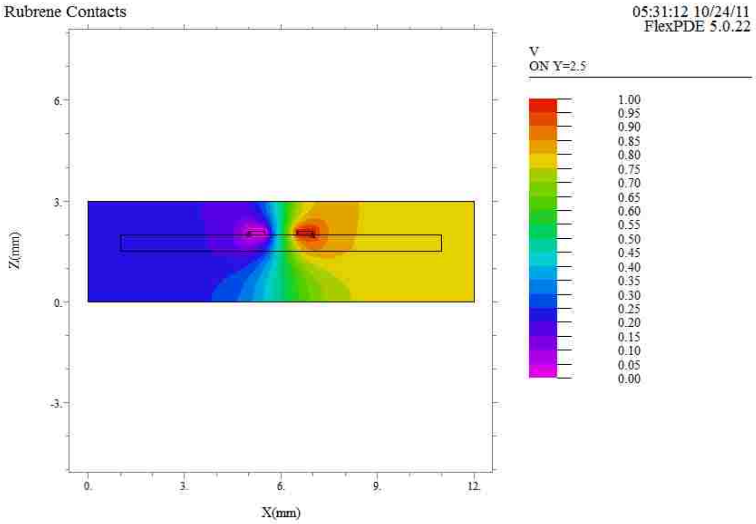

Figure 3.6: Electric Potential distribution in case of an increasing contact size

3.2 Increasing the size of the contacts

When we have a conventional configuration with two contacts positioned on the surface of the sample, it is possible to enhance the homogeneity of the electric field by extending the size of the contacts.

Figure 3.6 shows the electric field potential distribution. Further, the size of the contacts is increased outwards. Electric field for changing contact size is shown in Figure 3.7. The contact length increased from 1.5 mm to 2.5mm to 3.5 mm and then to 4.5 mm. The modeling in the region of interest, which is near the surface (from 0 to 0.1 mm), shows minimal reduction of the change of electric field with depth. Any extension of the contact has little effect, and as shown in Figure 3.5 only the distance between the contact seems to affect the change of electric field with depth.

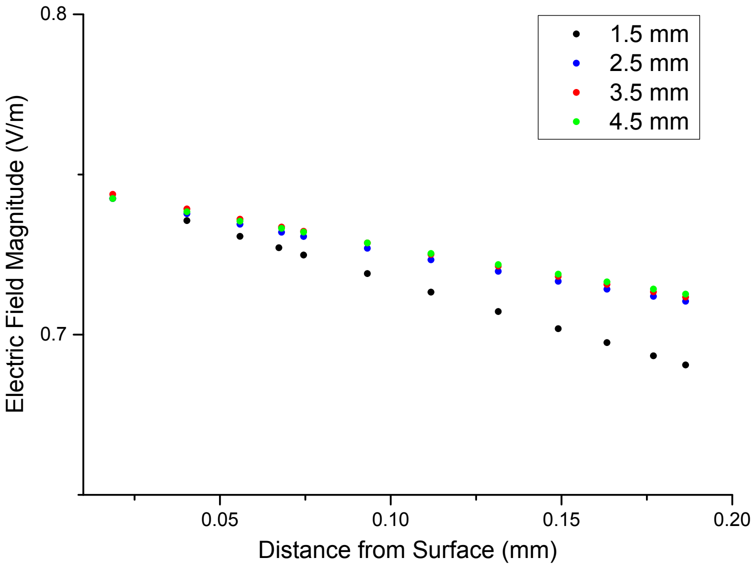

Figure 3.7: Electric field distribution in case of increasing contact size. The dielectric constant for the sample is 2.6, for the metal contact is 1e6, and for the surrounding air is 1. The same electric field near the surface was maintained. The thickness of the contacts is 100 μm. The default sample thickness is 300 μm. The length of the metallic contacts are 1.5mm, 2.5mm, 3.5mm, 4.5mm.

3.3 Effect of the sample thickness on the electric field distribution

Another possible way of improving the uniformity of the electric field is to use thicker samples.

As seen in Figure 3.9, discarding minimal variations created by numeric calculation artifacts, there is virtually no change by using different thickness samples.

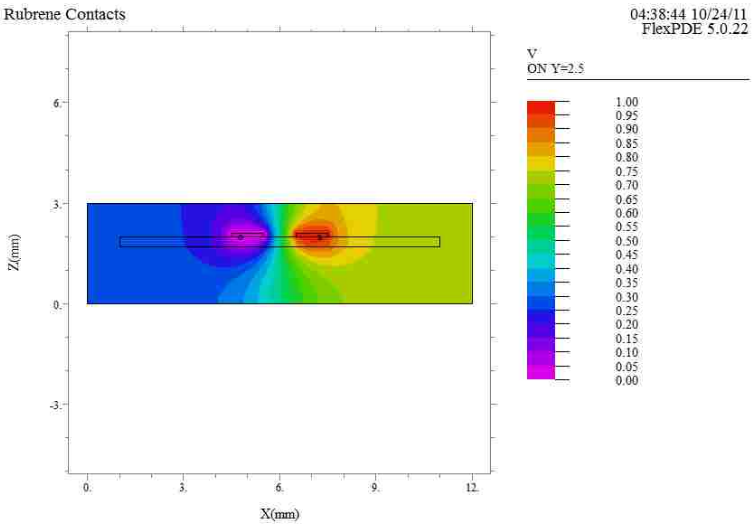

Figure 3.8: Electric potential distribution of various sample thicknesses

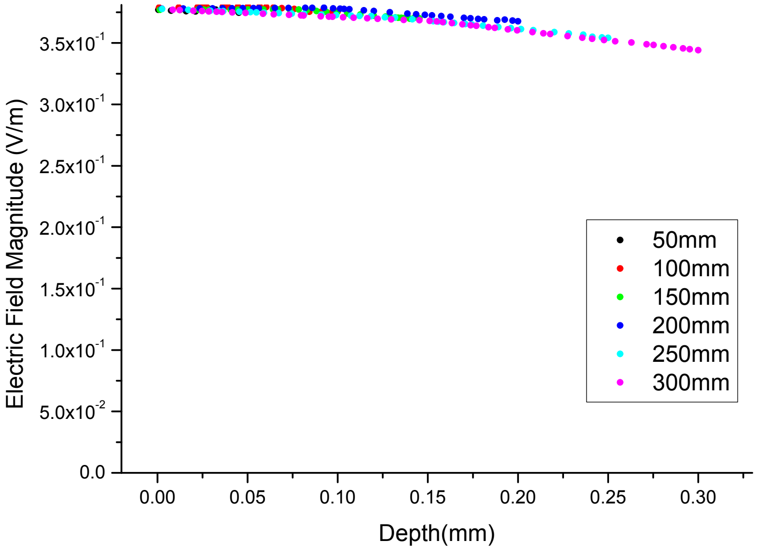

Figure 3.9: Distribution of of electric field for different sample thickness. The dielectric constant for the sample is 2.6, for the metal contact is 1e6, and for the surrounding air is 1. The same electric field near the surface was maintained. The thickness of the rubrene samples are 50 μm, 100 μm, 150 μm, 200 μm, 250 μm and 300 μm.

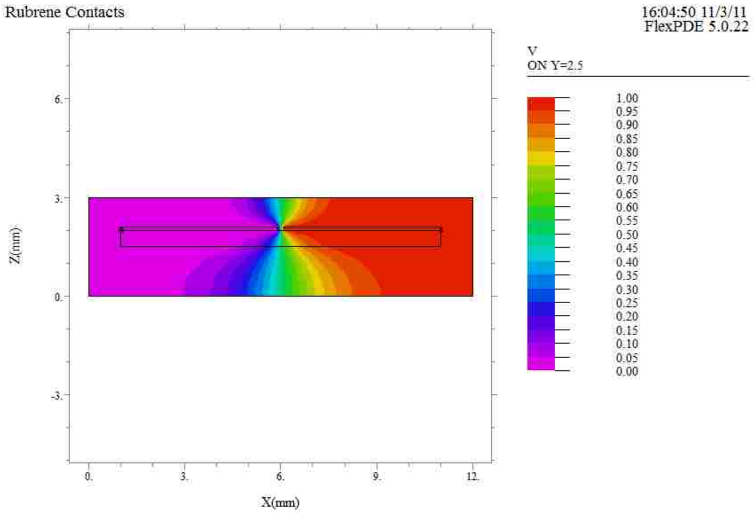

Figure 3.10: Electric potential distribution in case of a “slit” contacts geometry

3.4 Slit Contact System

Another popular geometric configuration is when the top of the sample is covered by contacts with only a narrow slit, where excitation by light can occur. This configuration allows to achieve maximum electric field strengths and to detect weak photocurrents.

In this configuration, the electric field results are in agreement with the previous calculations. The electric field distribution is highly dependent on the distance between the contacts. Although increasing the distance between the contacts (or in this case increasing the size of the slit) creates a slightly better electric field, its effect is minimal. One must highly take into consideration the electric field distribution when experimenting in this configuration.

It is to be noted that the above Figure 3.11 is similar to Figure 3.5. One should recognize that the distance used for Figure 3.11 is within a mm, which is comparable

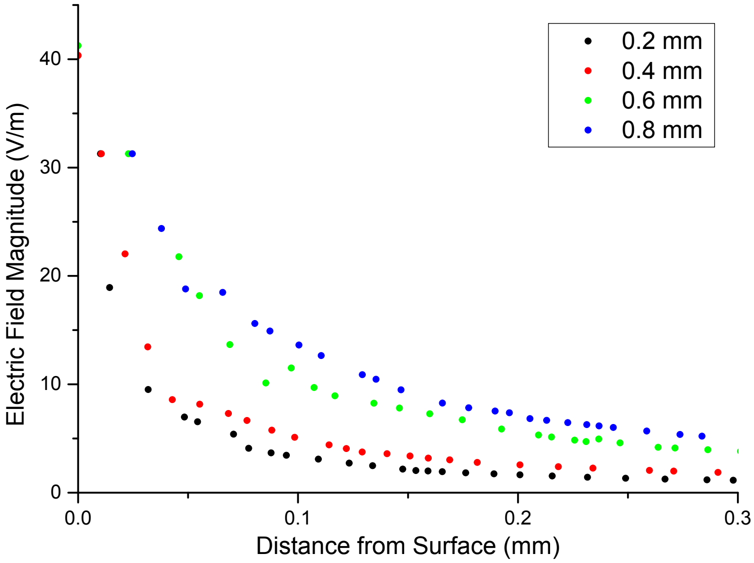

Figure 3.11: Electric Field in a “slit” contact geometry. The dielectric constant for the sample is 2.6, for the metal contact is 1e6, and for the surrounding air is 1. The potential difference between the contacts is 1 V. The thickness of the metallic contacts is 100 μm. The default sample thickness is 300 μm. The slit size (2d) is 0.2mm, 0.4mm, 0.6mm, 0.8mm.

with the 0.2 and 0.6 mm calculations in Figure 3.5 . Both calculations agree that only distance plays a major factor.

3.4.1 Electric Field at a distance from contacts

An alternative way of controlling the electric field strength is to conduct the measurement not between the contacts, but rather at a distance. If used properly, this configuration can excite regions of different electric field by simply moving the position of excitation.

In Fig. 3.15, the electric field decay into the sample is shown for 0.5 mm, 1.0 mm, 1.5 mm, and 2.0 mm horizontal distances from the contacts where the excitation occurs. In this configuration, control of the overall electric field magnitude can be

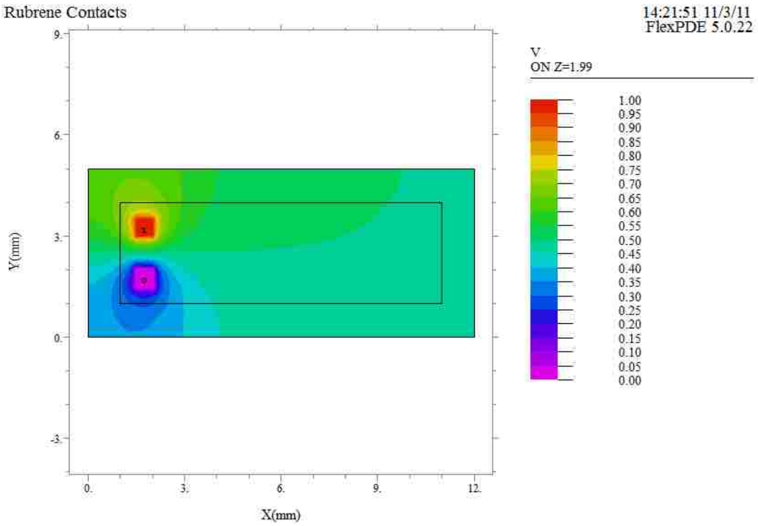

Figure 3.12: Electric Potential distribution at a distance from contacts

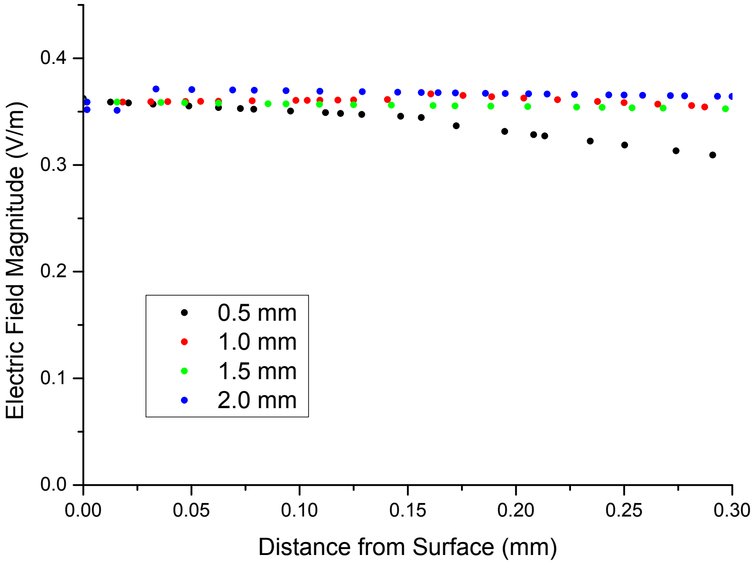

Figure 3.13: Electric field at different distances from contacts. The dielectric constant for the sample is 2.6, for the metal contact is 1e6, and for the surrounding air is 1. The potential difference between the contacts is 1 V. The thickness of the metallic contacts is 100 μm. The default sample thickness is 300 μm

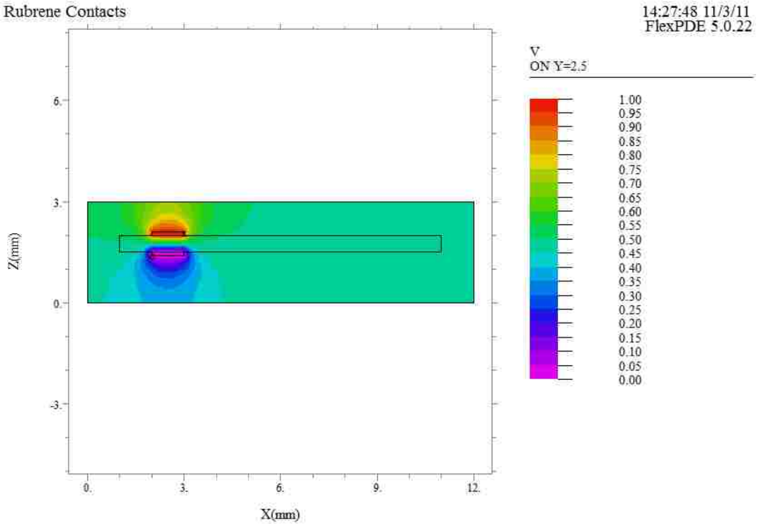

Figure 3.14: Electric Potential distribution of a Sandwich Contact System

achieved by moving the excitation position with regard to the contacts, and its electric field distribution change inside the sample shows to be negligible.

3.5 Sandwich geometry

Another common sample configuration is when one has contacts above and below the surface of the sample, so-called "sandwich" geometry. The excitation in this case occurs at some distance from the contacts. The electric field is obviously more complicated, and we focus only on the surface electric magnitude calculated with distance from the contacts.

We focus here on the electric field on the surface of the sample, and its dependence on the distance from the contacts. The electric field into the sample, which is not shown, varies rapidly predictably due to the potential difference created vertically into the sample, unlike the other configurations created horizontally.

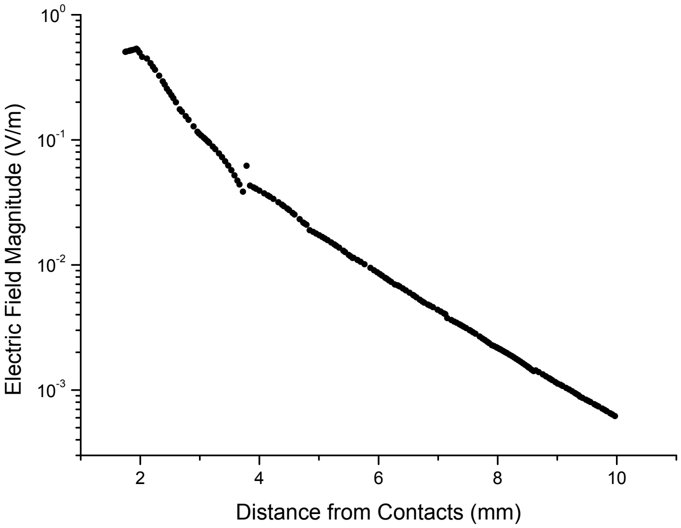

(a) Electric Field distribution of a "Sandwich Contacts" System. Here, the x-axis indicates the horizontal distance from the contacts on the surface, unlike previous calculations where the x-axis indicated the depth. The dielectric constant for the sample is 2.6, for the metal contact is 1e6, and for the surrounding air is 1. The potential difference between the contacts is 1 V. The thickness of the metallic contacts is 100 μm. The default sample thickness is 300 μm

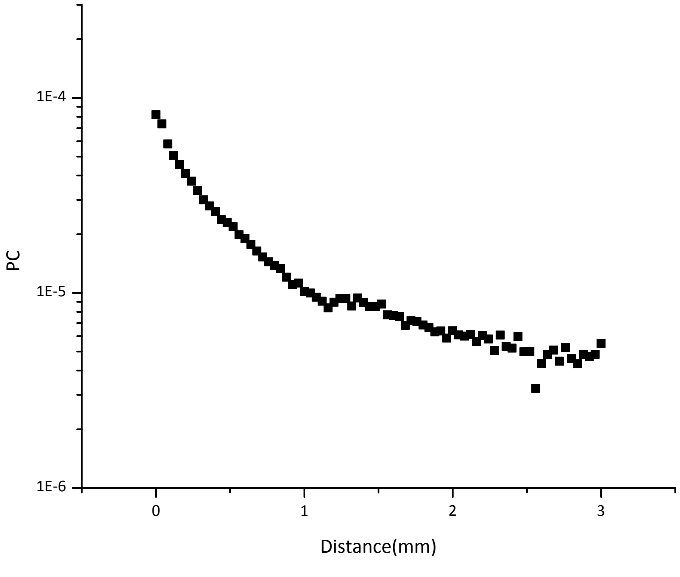

(b) Experimental Result of the Decay of Magnitude of Electric Field of a Sandwich Contact System. A constant pulsed laser was used to excite different positions on the sandwich configuration sample. The photocurrent was measured and expressed in log-log scale for comparison with the previous calculation on the electric field of a sandwich configuration.

Figure 3.15: Comparison of calculated electric field with experimental data

The calculations on the surfaces with respect to horizontal distance show that after some rapid decay, the position dependence of the electric field is nearly exponential, that is highlighted by a log-linear scale in the plot 3.15(a).

We can extract the electric field dependence on the distance from the contacts by using the same type of excitation at different points. Fig 3.15(b) shows a measurement of photocurrent as a function of the distance from the contacts. A strong similarity with the result calculated previously (Fig 3.15(a)) is present.

3.6 Conclusion

The creation of charge carriers by photoexcitation can occur up to 0.1 mm deep, thus we focus on mostly the first 100 μm. Out of all the possible methods of enhancing homogeneity, increasing the distance between the metallic contacts up to a 1mm only helped, any distance larger then that did not help much. Extending the contacts outwards or increasing the size of the rubrene sample did not help.

As a general calculation, when the distance between the contacts $2d$ vs the depth y has a ratio $2d/y = 20$, the electric field will decrease only 5%. For example, since most of our measurements are within $y = 100\mu m$, the distance between the contacts $2d$ should be 2mm to have a minimal electric field change of 5%.

In addition, the calculations on the sandwich configuration have shown agreement with the distance dependence photocurrent experiment, and this is a valid example that shows these calculations are reliable.

Chapter 4

Expectations for the photocurrent dynamics in light of the triplet exciton theory

In this chapter photoexcited excitons dissociating into charge carriers is discussed. Based on the previous model, we can also calculate the charge-carrier generation as a function of exciton dynamics.

Several assumptions are made for the calculation. First, singlets have a small probability of dissociation to free charge carriers. Second, triplets under some processes also have a small probability to create charge carriers. Third, the created free charge carriers are indistinguishable, and have a relative long lifetime. Fourth, charge carrier recombination, which is dependent on the charge carrier population density, is taken into account.

4.1 Defects as a meta-state for a different type of triplet dissociation

Although triplets are associated with charge carriers, the exact dissociation process is controversial. Two theories can be proposed for the two types of dissociation processes than can occur to triplets.

The energy of triplets is not large enough (about 1eV) to create charge carriers (about 2 eV) single handedly, and considering that the transition to the ground state for triplets is forbidden, their lifetime may be mostly determined by the interaction with defect states. Multiple types of defects in general can exist, but for simplicity one can propose a defect level that is dominant in creating charge carriers.

One can also consider singlet dissociation to charge carriers to be the exclusive process for charge carrier creation. In this assumption, the μs photocurrent should be proportional to the μs regime singlet population, which will increase quadratically with respect to the initial exciton population density. This is not the case [26], and only a linear dependence had been observed.

Therefore, another situation to consider is where two triplets contribute to one charge carrier creation through an intermediate level. (Another possible process with a single triplet will be discussed later.) One can consider excited trap levels: first, trap levels are occupied rapidly by triplets, then, additional triplets will have a certain probability of interacting with the occupied trap levels and create a state capable of creating charge carriers.

This process involves interactions of triplets with triplets. Since the limited number of trap levels should be occupied rapidly (if not, photocurrent increase quadratically), the interaction rate is determined by a fixed number of trap levels and the population density of triplets, which is proportional to the excitation power. The model will explain the linear relationship of excitation power to photocurrent. The sub-linear increase of photocurrent in high excitation powers are explained by the reduction of triplet population density through triplet-triplet fusion, which is independent from any processes involving traps.

We can also note that under extremely low excitation powers, when the population of triplets is comparable with the population of traps, the trap levels can consume the population of triplets leaving no free triplets left to interact with. In this case, almost no photocurrent is created, and the photocurrent increase should not be proportional to the excitation powers. Creating such experimental conditions with sufficient sensitivity to low currents is a very challenging task.

4.2 Rate equations for the meta-state model

As was done for semiconductors [2,27] we introduce a quadratic recombination factor into our rate equations.

$$\frac{dp}{dt} = -\gamma_{Np} N p - \gamma_{N_d p} N_d p - \gamma p^2 - \frac{p}{\tau_p} + 2\delta s, \tag{4.1}$$

where p is the population of triplets, N is the population of trap levels, N_d is the population of occupied trap levels, γ_{Np} describes how triplets interact with trap levels, $\gamma_{N_d p}$ describes how triplets interact with *excited* trap levels, γ is the triplet-triplet interaction rate, τ_p is the lifetime of a triplet, and δ is the conversion rate of singlets to triplets.

The amount of holes and electrons created through this model is,

$$\frac{dh}{dt} = +\gamma_{N_d p} N_d p - \gamma_{eh} e h - \frac{h}{\tau_h} \tag{4.2}$$

$$\frac{de}{dt} = +\gamma_{N_d p} N_d p - \gamma_{eh} e h - \frac{h}{\tau_e} \tag{4.3}$$

where γ_{eh} is the recombination rate of electrons with holes, τ_h is the lifetime of a hole. τ_e is the lifetime of an electron.

The change in the amount of the occupied trap levels and empty trap levels is

$$\frac{dN_d}{dt} = +\gamma_{Np} N p - \gamma_{N_d p} N_d p - \frac{N_d}{\tau_{Nd}} \tag{4.4}$$

$$\frac{dN}{dt} = -\gamma_{Np} N p + \gamma_{N_d p} N_d p + \frac{N_d}{\tau_{Nd}} = -\frac{dN_d}{dt} \tag{4.5}$$

where τ_{Nd} is the lifetime of an excited trap level.

The total population of trap levels has a constant value.

$$N + N_d = N_{tot} \tag{4.6}$$

N_{tot} is the total number of trap levels.

The rate equation for singlets is the same,

$$\frac{ds}{dt} = -\delta s - \frac{s}{\kappa} + n_s \gamma p^2 - l s \tag{4.7}$$

Thus with an initial exciton population density given as $s_0 = 10^6$, one can

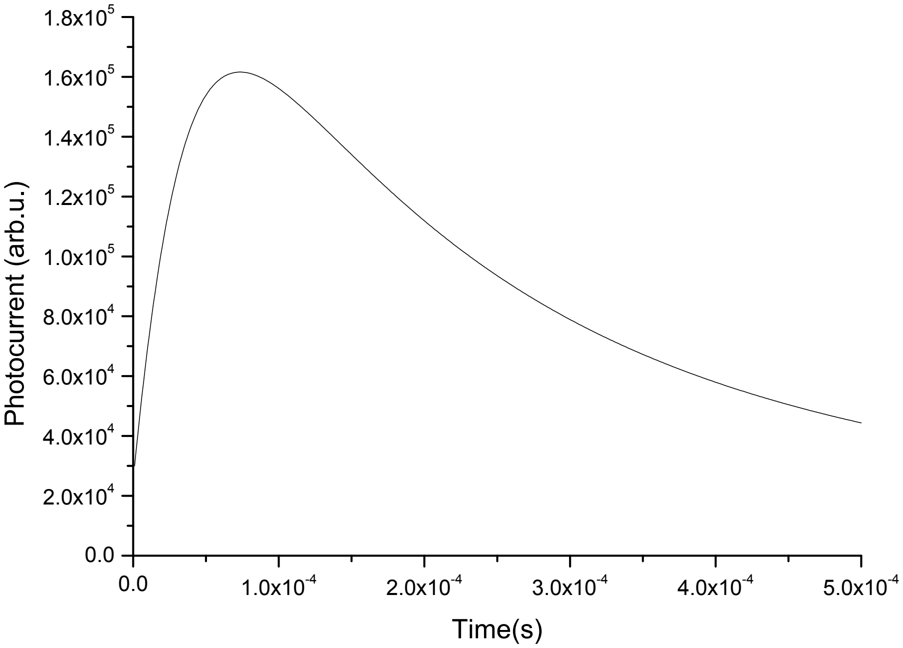

Figure 4.1: A calculation of a typical photocurrent using eq 4.2 is shown. The initial singlet population $s_0 = 40$, with $\tau_s = 10ns$, $\tau_t = 50\mu s$, $\gamma = 10^{-5}$, $n_s = 0.5$, $n_p = 0.5$, $\gamma_{eh} = 6 \times 10^{-2}$ are used.

calculate the hole density vs time,

In the calculation shown in Figure 4.1, one can observe a fast component right after t=0, then an increasing photocurrent till around t=100μs, followed by a decay with some lifetime of 0.5ms. The decay is a result of charge carrier recombination, without this, the lifetime is 6 ms.

Unlike hole densities, not much is understood for electrons. The calculation of holes is sufficient to explain the photocurrent dynamics, which could indicate electrons to have a short lifetime, or a small mobility [28, 29], therefore electrons will hide its existence in photocurrent observations.

Electrons could still play a role, and this will be discussed later.

4.3 Creation of holes by trap level electron affinity

Similar to Auger-like dissociation in semiconductors [30,31], another possible triplet to charge carrier dissociation mechanism is when high electron affinity trap levels interacts with triplets to create free holes. Based on a rather simple linear correlation between the photocurrent and triplet density observed in our experiments, one can think of such a more direct creation of charge carriers with the help of trap levels.

Photocurrent observations only detect total current and can not distinguish electrons from holes, but one can assume that the majority of photocurrent observed is due to holes, thanks to their large mobility as observed in rubrene, rather then low mobility for electrons [28, 29].

A trap level can then have a certain electron affinity which traps an electron, exciting and releasing the hole in the process. For this model to work, several restrictions should be included.

Since holes are created only when non-occupied trap levels exist, the total photocurrent is restricted by the number of trap levels available to triplets. But if the charge carrier dissociation process requires only a short amount of time, there is no reduction of the number of trap levels, and the photocurrent creation will be dependent on the number of interactions between triplets and trap levels. The higher the population of triplets, the higher the probability of interaction between triplets and trap levels. The probability of interaction will also depend on the rate at which triplets diffuse, thus one can expect that at higher temperatures a higher photocurrent would arise, which is in agreement with our experimental observations [32].

4.3.1 Rate equations for the electron affinity model

The rate equations for the electron affinity model is similar to the previous model, where the difference is that the interaction of excited trap levels is gone. The triplets and holes in this model are expressed with

$$\frac{dp}{dt} = -\gamma_{Np}Np - \gamma p^2 - \frac{p}{\tau_p} + 2\delta s \tag{4.8}$$

$$\frac{dh}{dt} = +\gamma_{Np}Np - \gamma_{eh}eh - \frac{h}{\tau_h} \tag{4.9}$$

There are no free electrons created through this model.

In this case the occupied trap level is different from the previous model ; The occupied trap level is not a bound triplet that may interact with another triplet, rather, it is a bound electron in this model. (The same notation is used for convenience.)

$$\frac{dN_d}{dt} = +\gamma_{Np}Np - \frac{N_d}{\tau_N d} \tag{4.10}$$

$$\frac{dN}{dt} = -\gamma_{Np}Np + \frac{N_d}{\tau_N d} = -\frac{dN_d}{dt}, \tag{4.11}$$

where the total population of trap levels is still constant, and the rate equation for singlets is the same as above.

In general, the first model (where the trap level acts as a meta-state) is somewhat similar to the other model of a short-lived trap level of high electron affinity. The hole density rate equations 4.2 and 4.9 are equivalent when

$$\gamma_{N_{dp}} N_d = \gamma_{N_p} N \tag{4.12}$$

$\gamma_{N_{dp}}$ and γ_{N_p} are constants, but the trap population densities N_d and N are not. In certain conditions such as when τ_{Nd} is small, photocurrent will not be proportional to the initial exciton population density. Here, we focus on conditions that maintain the linear dependence with the initial exciton population density vs. photocurrent, as observed in [26].

4.3.2 Similarity of both models

When,

$$\tau_{Nd} \gg 0 \tag{4.13}$$

and,

$$\gamma_{N_{dp}} \gg \gamma_{N_p} \tag{4.14}$$

The majority of trap levels are not populated, so we can consider N as a constant value. Thus, Equations 4.2 and 4.9 are simplified where the terms $\gamma_{N_{dp}} N_d$ and $\gamma_{N_p} N$ are constants.

Both models can create photocurrent that increase linearly with the corresponding triplet population. A major difference is in the output of charge carriers: an electron-hole pair from the meta state model, and just a single hole from the electron affinity model.

As the mobility of electrons is around 0.3 cm^2/Vs, whereas it is 0.8 cm^2/Vs for

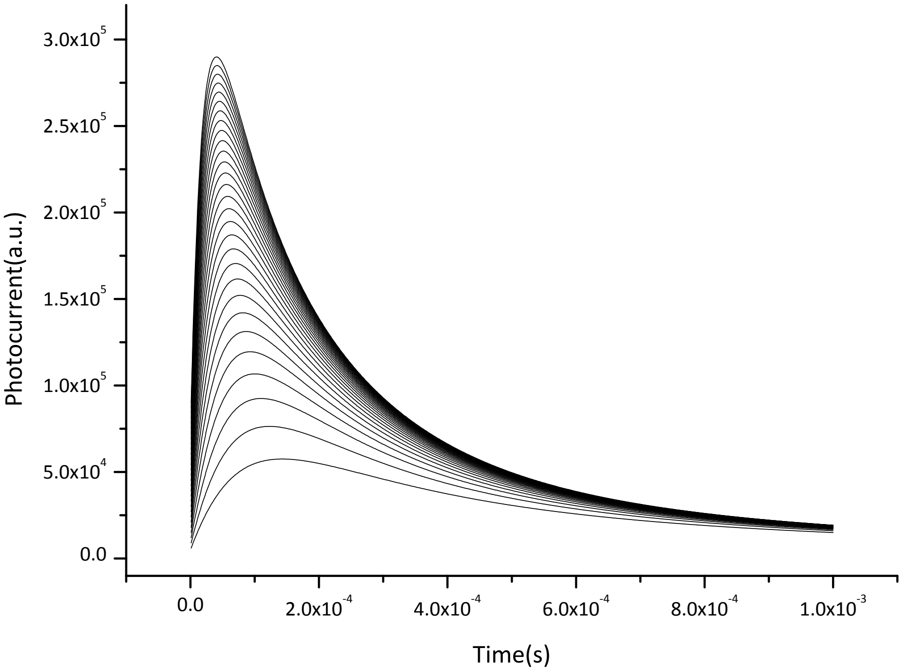

Figure 4.2: The photocurrent was calculated when the triplet lifetime was 100μs, charge carrier lifetime 6 ms, quadratic coefficient for triplet-triplet fusion 10^{-2}, quadratic coefficient for charge carrier recombination 6×10^{-2}

holes [33], we simply consider holes to be the major contributor to the current. The triplet population is achieved according to the rate equations for triplets, 2.2 and 4.7. Then the hole population density is obtained from Equations 4.2 and 4.9.

4.4 Numerical calculation of the photocurrent

By using Equations 4.2 and 4.9, we can see how the photocurrent dynamics will change with different initial exciton populations.

Figure 4.2 shows the change of photocurrent dynamics with different excitation power. The curves show the stronger the excitation, the larger the magnitude of the photocurrent. Another thing to notice is the shift of the photocurrent peak,

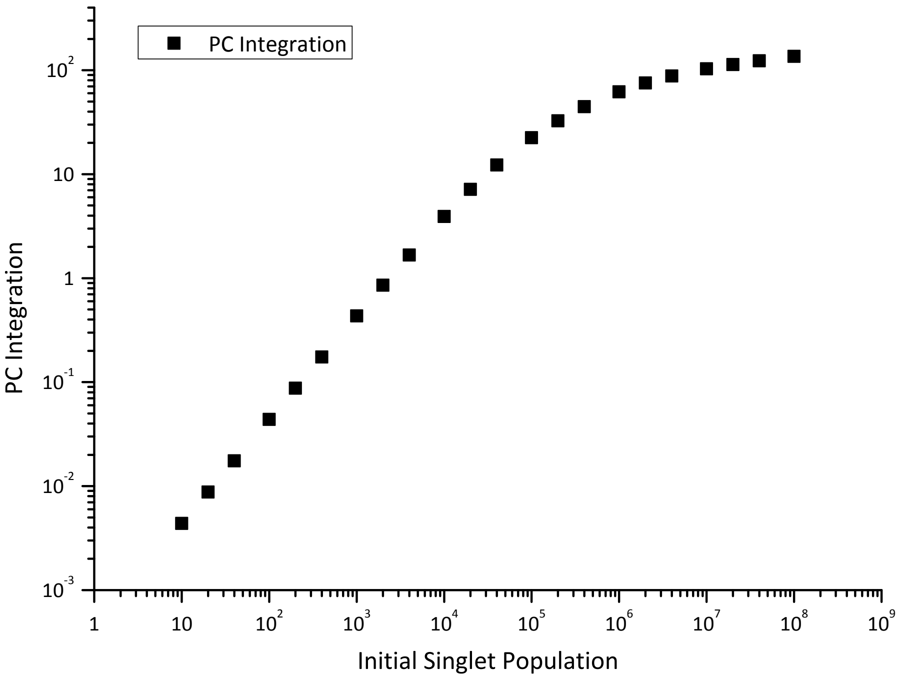

Figure 4.3: Integration of various photocurrent simulations. The initial triplet population varied between 10 and 10^8.

previously explained by the faster depletion of the supplier of photocurrent. The magnitude increase is suppressed due to triplet-triplet fusion, which also explains the reduction of the build up time. The rapid decrease is explained by a quadratic recombination of charge carriers expressed as $\gamma_{eh}eh$ in Equations 4.2 and 4.9. If a quadratic recombination would not exist, the decays should have been similar, with consistent exponential decay corresponding to a lifetime of the charge carrier.

In order to see how many charge carriers are created with different initial exciton populations, we can take the integral of photocurrent shown in Eq. 4.3.

The population of charge carriers is affected by quadratic recombination of triplets and also of charge carriers. The quadratic recombination of triplets control the total amount of photocurrent as well as the build up dynamics. Charge carrier recombination kicks in at much higher (initial exciton population) densities, and contribute to the shortening of the photocurrent lifetime.

In Figure 4.3 in a region where only one quadratic function (triplet fusion) applies, one can observe a slope 2 in log-log scale, which is equivalent to a root two increase in linear scale. But once both effects work simultaneously, the quenching becomes much more severe.

4.4.1 Shortening of photocurrent buildup time

A strong observable feature of the photocurrent is its buildup time. For longer time regimes, analysis is harder due to a significant decay of charger carriers, thus it is easier to observe the build up, where the photocurrent is highly dependent on the triplet population.

With different initial populations of excitons, we can see Figure 4.2 that the required time for the individual photocurrent curve to reach its maximum is different. To compare with experimental data, one can keep track of the time required to reach 20%, 50%, and 80% of its photocurrent maximum.

By plotting the reciprocal of the time required under different initial conditions, we can recognize the shortening of this time occurring at different magnitudes. It changes from a constant value to different values when triplet-triplet interactions begins to play a role, i.e. when a change in build up dynamics is observed by Eq. 4.2.

4.4.2 Meta-state model calculations

Though the two models introduced above both work in optimal conditions, there are limitations to each model that needs to be addressed. This will help choose

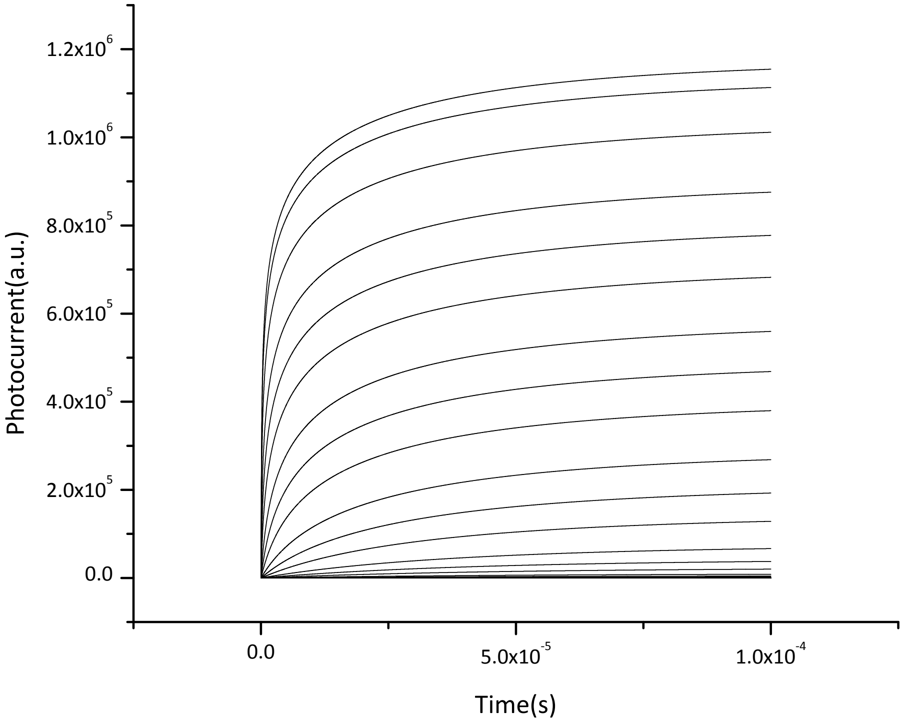

Figure 4.4: The photocurrent was modeled with various initial singlet densities $s_0 = 1, 2, 4, 10, 20, 40...., 2x10^{13}$.

the more probable model. Calculation-wise, both models are similar when γ_{Np} is sufficiently large, so we focus on the meta-state model.

In order to see any bottleneck effect, or saturation due to the meta-states that create charge carriers, we assign the maximum trap population to a relative small value of 10^5. We then use Equations 4.2, 4.4, 4.5, and 4.7 to calculate the photocurrent on various initial singlet population densities.

In Figure 4.6, as the initial singlet population density increases, the limited meta-states start to saturate. This works as bottleneck for charge carrier creation, and thus reduces the photocurrent magnitude. On lower densities, the photocurrent

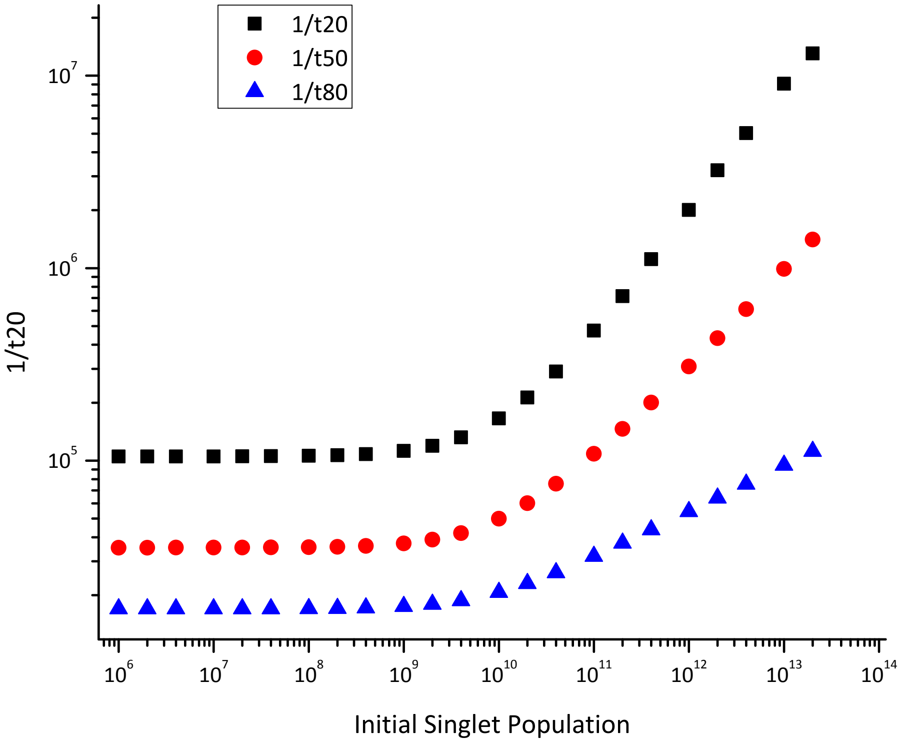

Figure 4.5: The reciprocal of the time required to reach 20, 50, and 80 percent of the photocurrent maximum is shown for various initial singlet densities $s_0 = 1, 2, 4, 10, 20, 40...., 2x10^{13}$.

increases quadratically. This is due to the increase in triplet population that contribute to the increase of the interaction creating meta states and the interaction of meta states that creates charge carriers. When the initial population $s_0 = 10^7$ increase to $s_0 = 10^8$, which is 10 times, the photocurrent increases 100 times. But once the meta states are saturated, when the population $s_0 = 10^{10}$ increase to $s_0 = 10^{11}$ the increase of photocurrent is drastically reduced to a sub-linear increase.

Since Figure 4.6 shows triplet-triplet fusion and also charge-carrier recombination effects, it might mix with the saturation effects and shadow understanding of photocurrent at high densities. Therefore we conduct another calculation that

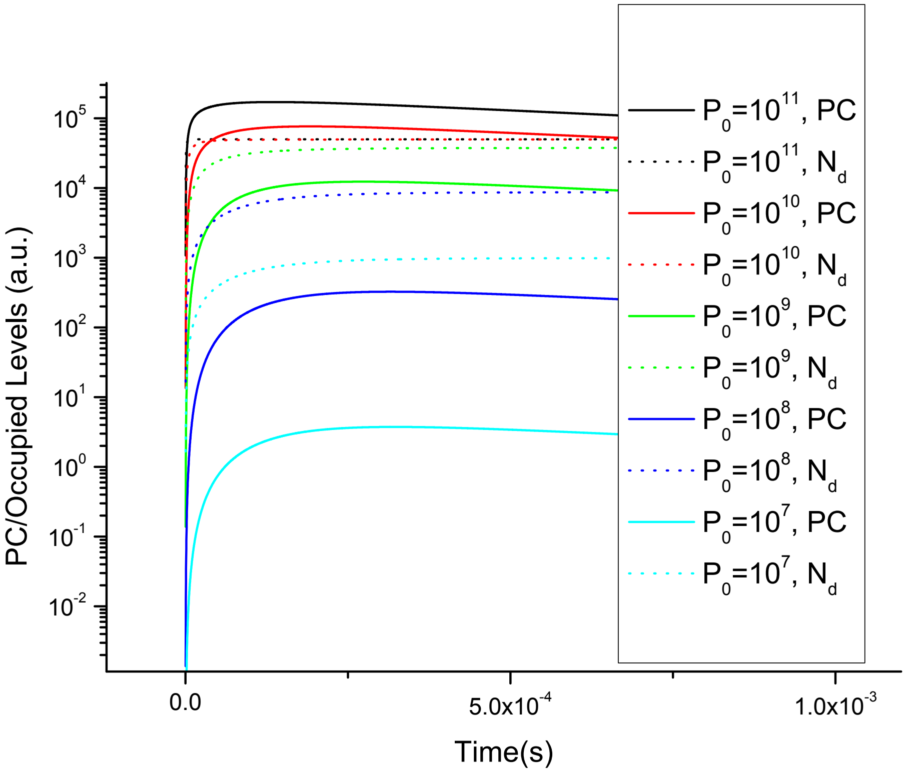

Figure 4.6: The photocurrent dynamics are calculated in the regime when the meta state starts to saturate. The initial singlet densities are $s_0 = 10^7, 10^8, 10^9, 10^{10}, 10^{11}$. The interaction rates are $\gamma_{Ndp} = 10^{-5}, \gamma_{Np} = 10^{-5}$.

excludes both quadratic effects, to understand how the meta-state saturation will affect photocurrent increase.

In Figure 4.7 with all quadratic effects removed, photocurrent increases quadratically when the meta-states are not saturated. This can be seen when $s_0 = 10^7$ increases to $s_0 = 10^8$. At higher densities when $s_0 = 10^{10}$ increases to $s_0 = 10^{11}$, the meta-states are saturated and the photocurrent increase linearly.

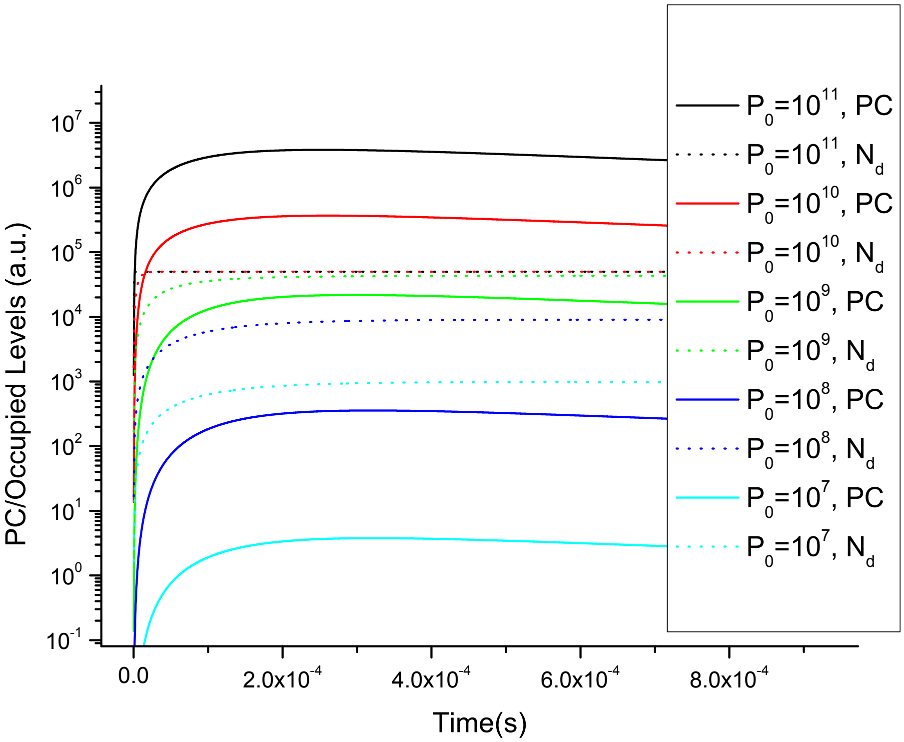

Figure 4.7: The photocurrent dynamics are calculated in the regime when the meta state starts to saturate. The initial singlet densities are $s_0 = 10^7, 10^8, 10^9, 10^{10}, and 10^{11}$. The interaction rates are $\gamma_{Ndp} = 10^{-5}, \gamma_{Np} = 10^{-5}$. The triplet-triplet fusion interaction rate γ is now zero and no triplet fusion occurs.

4.5 Conclusion

We have introduced two models that can explain charge carrier dissociation by triplets. Besides the existence and in-existence of free electrons, models will result in the same hole population density, which will create the same photocurrent. The electron affinity model is simpler, and easily explains photocurrent dynamics. The meta-state model might result in a quadratic increase of photocurrent, which was not observed. However when the trap level population N is small, or when the interaction rate between the trap levels with triplets γ_{Np} is large, the meta-state is saturated. This effectively work similar to the electron affinity model, resulting in similar photocurrent dynamics.

Both models work, but the meta-state model predicts super-linear increase of photocurrent in low densities. This was not observed, and the restrictions required for this absence explained above makes this model less probable then the electron affinity model. The electron affinity model may also show a saturation of photocurrent increase, when the excited trap levels have a long lifetime. However, this has not been observed yet, and the electron affinity model seems to be slightly more probable.

It is to be noted that in our models, photocurrent was proportional to the (unoccupied) trap level population densities N. For example, experimental-wise, a long exposure of rubrene samples (several months to a year) in air resulted in an increase of photocurrent, and additional exposures (after several years) resulted in a photocurrent decrease. The increase and saturation of the amount of different trap levels with time can be taken to account, where different trap levels can contribute to photocurrent [34] or simply reduce the lifetime of triplets. It is yet difficult to fully explain the observed behavior, but one can correlate the amount of trap levels to the efficiency of the creation of photocurrent.

Chapter 5

Experimental observations of photoluminescence and photocurrent in rubrene

With the triplet model described above, the dynamics of the photoluminescence under various initial conditions can be predicted. The experimental results and comparisons for the confirmation of the model are presented.

5.1 Experimental Setup

5.1.1 Rubrene samples

A typical rubrene single crystal sample used has two silver contacts on a top to produce an electric field inside the material. The photoexcitation and collection of the luminescence occur in the middle of the sample, which is normal to the bc facet.

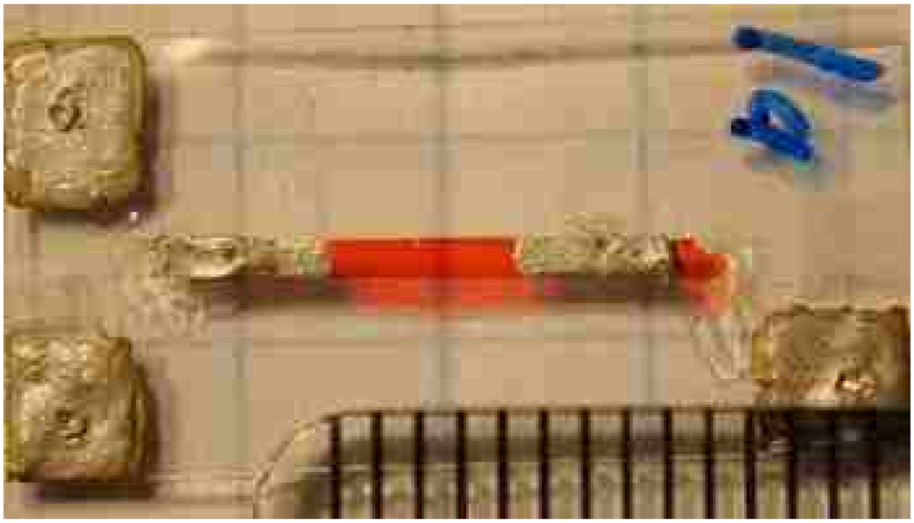

Figure 5.1: Various sizes and shapes were used, but a typical sample is 1 cm long, 1 mm wide, and a couple hundred microns thick.

An electric voltage is applied ranging from a couple volts to 2000 V. Our experiments are executed in room temperature with full exposure to air. The samples are very stable in normal conditions. Only after a year under exposure in air will there be a noticeable change in the measurements.

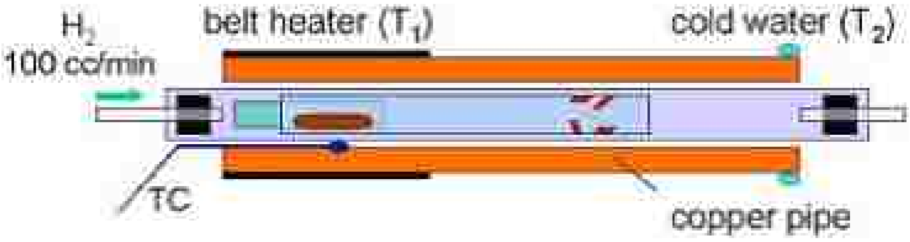

Figure 5.2: Rubrene single crystals used in the measurements were grown by Physical Vapor Transport method [2,8], which utilizes a horizontal heated tube with a gas flow. High temperature ($300°C$) Ar, He, and H2 gases flow while maintaining a temperature gradient in a heated tube with raw rubrene.

The crystal samples are grown by Physical Vapor Transport method, which is an effective method of constructing weakly bound organic crystals. Although the purity of the crystals will affect the density of trap levels that could create different oxidation and trap levels distributions and densities [35], PVT for rubrene have shown to create pure crystals [36] in general. All samples were grown by the same method with the same equipment to maintain consistency.

5.1.2 Laser system

The main laser system used in the experiments was PL2143A EKSPLA Nd:YAG laser operating under passive mode locking conditions. The laser is composed of a master generator with an additional regenerative amplifier, optical pulse amplification, and harmonic generation. The fundamental wavelength of the Nd:YAG is frequency doubled, tripled and quadrupled by letting the beam pass through the nonlinear crystals to create 1064, 532, 355, and 266 nm output wavelengths. The repetition rate was 10 Hz (which was essential in order to observe events that take longer than miliseconds).

5.1.3 OPG

In these experiments, an Optical Parametric Generator (OPG) was used to control and select any wavelength within 430-680 nm and 740-2300 nm. The 355 nm pump laser from the Nd:YAG laser was collected with only a pulse energy of 8mJ. The maximum output energy per pulse was 300 μJ. Due to the nonlinear behavior of the OPG, the observed laser output had a small fluctuation of less than 5%.

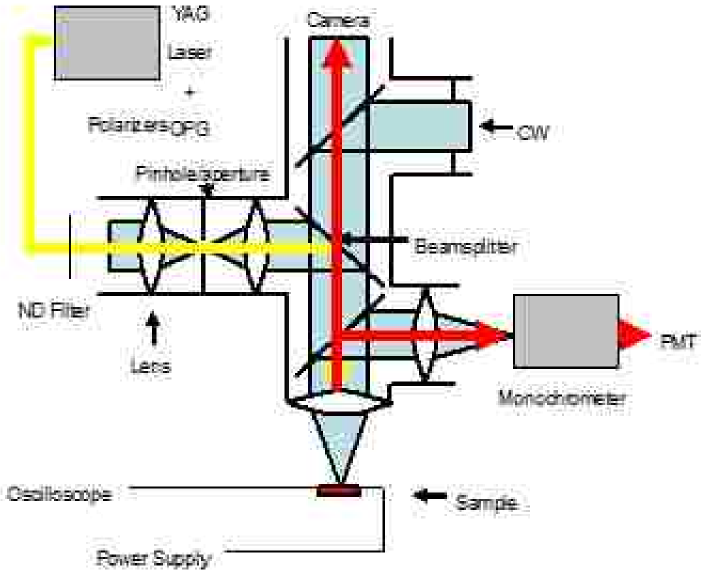

Figure 5.3: Microscope used for Photocurrent and Luminescence Measurements.

5.1.4 Microscope

Because controlled positioning of the excitation, and calculation of the photon density is crucial, a custom built confocal microscope was used for measurements. As the laser pulse approached the setup, the laser power was controlled by 2 polarizers. An ND filter was also used when extremely low powers were desired. The laser light was focused onto a pinhole of various sizes (from 10 to 500μm in diameter) with a scattering element. The laser was then collimated with another lens with f=25.4 mm. Thereafter a microscope objective was used to focus the light onto the sample. The microscope also allowed a separate pathway for a CW light, and another pathway for luminescence measurements. A CCD camera was attached above to check the position of excitation, and also the quality of focusing. The observed pulse energy had a maximum of ˜150 μJ when it reached the sample.

5.1.5 Various Sample Configurations

5.1.6 Detection

The circuit was connected to a Lecroy Waverunner 4 GHz oscilloscope with input impedance at 50Ω (for measurements requiring response times of about 1 ns) to 1 MΩ(for better signal to noise ratio, in conditions that do not require fast response time), or in between.

Another important observable is photoluminescence. The luminescence created by the sample followed either a path that was focused to a monochromator connected to a photomultiplier, or to a usb2000 OceanOptics spectrometer, which had a detection range of 200-1100 nm with a resolution of 1-3 nm. An additional path for CW lasers or white light was available while excitation by the pulse laser was occurring.

5.1.7 Experimental Procedure

The purpose of the experiments was to understand charge carrier behavior in rubrene single crystals by using impulsive laser photoexcitation to create excited rubrene molecules.

The primary excitation laser (introduced above) provided an excitation wavelength between 430-2300 nm. The laser output power was kept constant, and the excitation power was controlled with external polarizers and ND filters. The location and focusing of the excitation was monitored by a CCD camera attached above the microscope. The rubrene sample itself is fixed on a transparent plastic substrate. The stage and the sample were enclosed in a Faraday cage for better signal to noise ratio due to the high sensitivity of the setup to external fields. An electric field was applied on the sample to measure the photocurrent with an oscilloscope. The luminescence was measured simultaneously and independently with the optical path which sent the light directly into a spectrometer or monochromator connected to a PMT. The tunable variables existing were: laser power/wavelength/polarization, excitation position/size, electric field strength/distribution, and sample temperature/size/thickness.

One of the main reasons for constructing a new setup was because of the large noise in our earlier measurements. The dominant noise present was created by the laser triggering electronics, but this was overcome by recording the noise created without any excitation on the sample. This was possible since the noise from the electronics was synchronized with the laser pulse. Other sinusoidal noise suspected to be created by other strong electronics or machines nearby was observed, but by adjusting the averaging, it averaged out to a minimum. For photoluminescence measurements, scattered laser light was the dominant source of noise, but proper filters and alignment helped suppress the noise.

5.2 Observation of Luminescence of a Rubrene Single Crystal

Previous observations [37] have shown that after impulsive photoexcitation, most of the luminescence of rubrene decays within 10 ns. A small remnant luminescence was also observed at time scales of a few μs, but no functional form of this decay was identified due to the lack of data.

Before detailing our observations, one can argue about the delayed luminescence origin, and consider the possibility of it is created by an intermolecular energy level with an extraordinary lifetime, rather than by mobile interacting triplets. To prove that the crystalline structure plays a key role, the following two can be compared: the luminescence from rubrene molecules dissolved in a solution (to minimize interaction between molecules), and the luminescence from rubrene molecules in a single crystal.

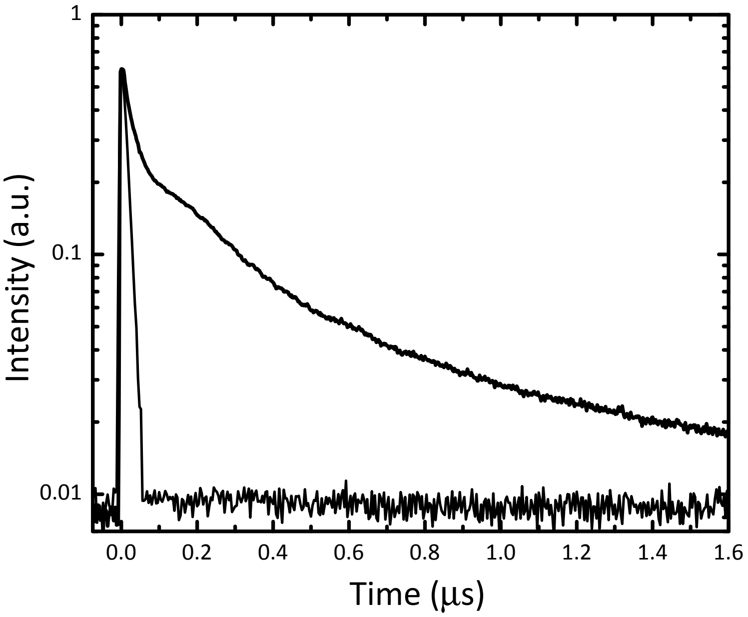

Figure 5.4: Comparison of luminescence decay of rubrene in solution and in a single crystal. The excitation was controlled to ensure that the total number of absorbed photons were similar in both cases. The crystal luminescence showed a significant amount of delayed signal which was not the case in solution.

As can be seen in Fig. 5.4, no significant μs luminescence existed for rubrene in solution form. A similar ns decay was observed for the single crystal form.

In Figure 5.4 the solution form shows a longer lifetime then the crystal form. This is consistent with the fact that singlets in a crystal have an additional transition to triplets available. Integrating the luminescence signal indicated that the delayed luminescence was larger than the nanosecond luminescence. This shows that the efficiency of transition to triplets is larger than a direct intermolecular decay.

5.3 Long-lived luminescence

A large difference noticeable in the μs scale is in agreement with Ref. [38].

The existence of this μs luminescence signal in rubrene single crystals indicates the presence of some energy state which is directly linked to the crystalline structure. Considering its long lifetime, triplet excitons have been proposed as identification of this long-lived energy state.

Since the model predicts that interaction between triplets is highly dependent on the exciton population density, we predict the luminescence observed show different time dynamics depending on the initial exciton population density. This initial exciton population density is determined by the absorption constant of rubrene for the corresponding excitation wavelength, polarization, and the power of excitation.

Previous measurements have shown that while increasing excitation energy, the ns luminescence increased linearly [32], also commonly observed in other organic crystals.

In order to validate the μs luminescence decay existence and its characteristics, we shall now focus on the μs time scale. The following data was achieved with an illumination spot size of 2 mm in diameter, by 20 ps, 40 μJ laser pulses at 10 Hz, produced by Ekspla optical parametric generator. [23]

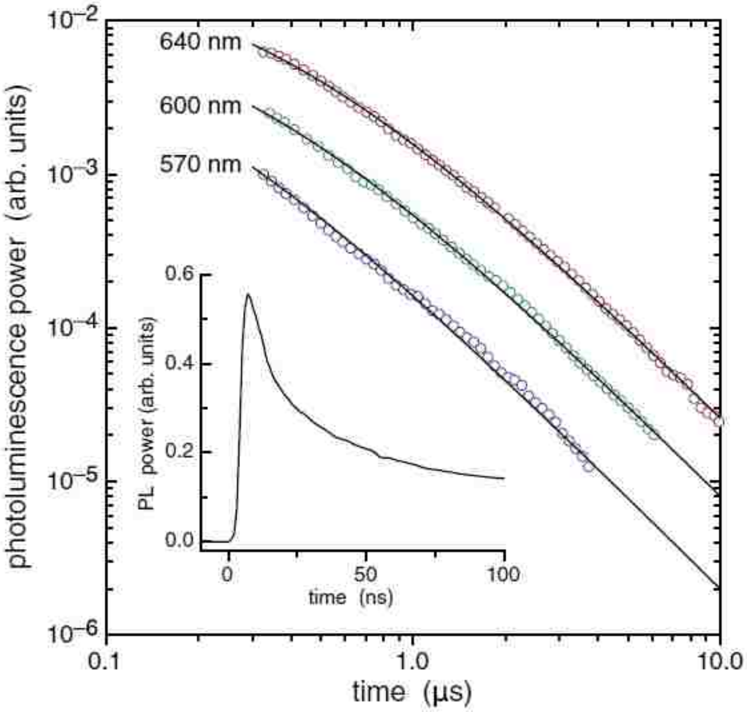

Figure 5.5: The luminescence of rubrene excited by various light wavelengths are shown in the μs scale. The inset shows the luminescence in ns scale. From Ref [23]

Due to the difference in absorption constant, controlling excitation wavelength allows several magnitudes of difference in population density, without directly controlling excitation power. In the above experiment, 5.5, we present the luminescence decay of rubrene with 640 nm, 600 nm, and 570 nm detection. With adequate excitation power, a t^{-2} relationship is observed. When plotted, in a log-log scale the slope of the straight line is -2, just predicted by model 2.3.

Figure 5.6(b) compares different levels of excitation applied to rubrene. As predicted by the model Figure 2.3, the high excitation luminescence decays much more rapidly, reaching the t^{-2} relationship (slope of -2 in this log-log scale), whereas

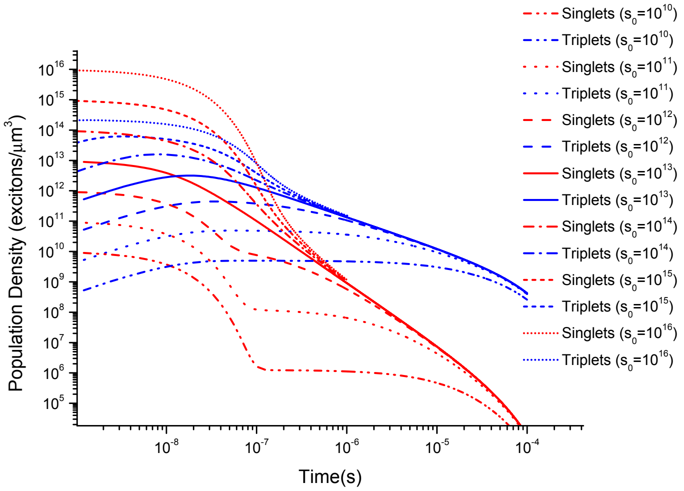

(a) Figure from 2.3. In the microsecond regime, higher excitations resulted in a more straightforward quadratic decay.

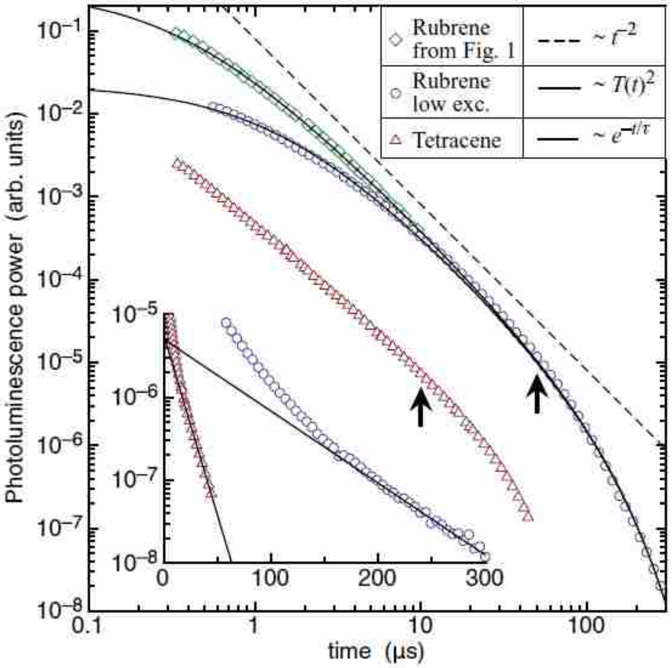

(b) Luminescence in Rubrene and Tetracene for different excitation levels. The luminescence is shown for rubrene with high and low powers of 530 nm excitation. The luminescence of tetracene with high power of excitation is shown for comparison. From Ref [23]

Figure 5.6: PLAnalysis

the lower excitation approaches this slope later. Also as seen in Figure 2.3, when the population density decreases to a certain value that the effect of the lifetime of triplets is comparable or more dominant than the fusion of triplets, we observe an exponential decay plotted as a curve with increasing slope in this log-log scale. In the inset of 5.6(b), the luminescence of tetracene is plotted against rubrene in a log-linear scale.

5.4 Photocurrent observations

Organic molecular crystals have various excitonic states that are rather complex [39–41]. We have observed a delayed photocurrent, which increases after impulsive photoexcitation up to about 100 μs, and then decays according to the charge carrier lifetime [37]. We identified a fast photocurrent component [26], which is commonly observed in other organic crystals [42], and this fast photocurrent is well described in rubrene single crystals [42–44].

Based on the similar lifetimes [23], one can propose that the triplet excitons [14, 19, 45–47] are these long-lived energy states [32].

One can also assign singlets created by triplet-triplet fusion to be the contributor to the charge carriers in the long time regime, based on the observation of the fast (ns) creation of charge carriers after impulsive photoexcitation. Previous observations of photoluminescence are in fact a very direct probe of the singlet population. If the singlets were the main source of the charge carrier creation, and the charge carrier lifetime was observed to be relatively long, the photocurrent must then be proportional of the singlet population. However, this is not supported by experimental observations [48].

In low power regimes, the photocurrent dynamics does not change with excitation powers, and the only change observed was the proportional increase of the photocurrent magnitude. If the contributor to the delayed photocurrent was singlets created by triplet-triplet fusion, one would rather observe a change in photocurrent dynamics because of the significant “quadratic” contribution of the triplet-triplet fusion. The proportional, linear increase of the photocurrent amplitude indicates that the charge carrier creation must be directly related to the triplet exciton population.

The creation of charge carriers from singlets in our experimental conditions had very low efficiency, whereas the fission of singlets to triplets have a much larger probability. If creation of charge carriers was dominantly from singlets, one should expect a strong fast current component from the very large population of singlets right after impulsive photoexcitation. Rather, the delayed photocurrent was about ten times stronger than the fast photocurrent. Charge carriers that could be created by singlets in the 100 μs regime is not overlooked, but its contribution is very small, and can be ignored when understanding dominant sources of delayed photocurrent.

5.4.1 Photocurrent dynamics in low excitation power case

Under low excitation power conditions, the population of triplets is not affected by the triplet-triplet fusion. The decay of triplet population is dominated by the triplet lifetime, which will produce a typical exponential decay dynamics. The long charge carrier lifetime and the photocurrent directly produced from triplets (which is an integration of an exponential) result in an exponential increase of photocurrent with time. Hence, at low excitations, a linear increase of excitation power up to a certain point may still correspond to a situation where no triplet-triplet fusion would affect triplet population, and the photocurrent dynamics would only change in magnitude. These expectations have been already confirmed [32].

5.4.2 Photocurrent in case of high excitation powers

The behavior of photocurrent becomes more complex in higher excitation power case, when the triplet-triplet fusion process starts to dominate the decay process of the triplet population. The photocurrent, which effectively under a long charge carrier lifetime, is an integration of this decay. The photocurrent increase vs. time will move away from a simple exponential increase, and will become more rapid. This explains the shortening of buildup time observed [32]. Due to the fact that the charge carriers are directly created by triplets, and the triplet population decay dominantly through triplet-triplet fusion, the triplet population that contributes to the creation of charge carriers will be suppressed in this case.

5.4.3 Absorption and Luminescence Spectrum of rubrene single crystals

Before we present the results of the photocurrent measurements, we must keep in mind the fact that due to the difference in absorption constants, the exciton population created by each corresponding excitation wavelength can differ up to several orders of magnitude. An absorption and emission spectra of rubrene is plotted in Figure 5.7.

The highest absorption occurred at 497 nm, and the multiple peaks correspond

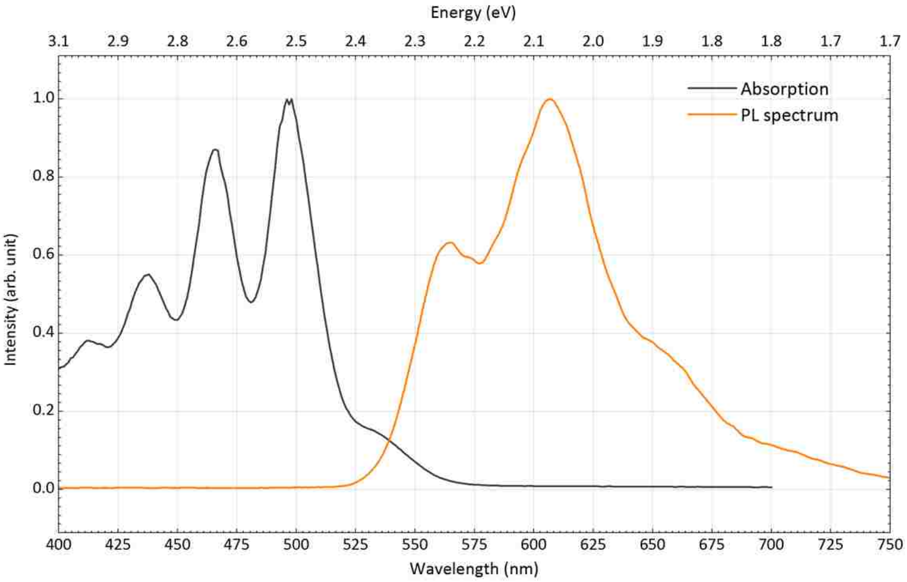

Figure 5.7: Absorption and PL Emission Spectrum of a Rubrene Single Crystal collected from the ab facet. Absorption spectrum was measured with light polarized along the b-axis, propagating normal to the ab facet.

to vibrational levels. The first excitonic level was located at 530 nm. The PL emission collected from the ab facet peaked at around 610 nm. All measurements were conducted with b-polarized excitation normal to ab facet. It must be emphasized that the absorption at the ab facet is relatively weak, whereas for bc facet (for c-polarized light) the absorption coefficient is an order of magnitude stronger, given the dipole transition parallel to the c-axis [24]. All excitations and emission measurements were conducted only on the ab facet for consistency and for experimental convenience, because most rubrene crystals have a large ab surface, and the mobility of holes was found to be strongest along the b-axis. In the fixed experimental conditions, the absorption for all excitation wavelengths is known, and this absorption is needed to calculate the exciton density created at each excitation wavelength.

5.5 Photocurrent Dependence on Wavelength and Power of Excitation

In Fig. 5.8(b), power dependent and wavelength dependent photocurrent measurements are presented. On the left, the excitation energy, or in other words, the individual 20 ps pulse energy changes, from 0.03 μJ up to 18 mJ. In agreement with our model, when the exciton population density is small when almost no triplet-triplet fusion occurs, the photocurrent magnitude increases linearly, with no change in dynamics. This can be seen in the first few low-power curves in 5.8(b).

At some point the exciton population density is large enough so that the triplet-triplet fusion has a large enough effect on the decay of triplets in rubrene, effectively reducing the amount of triplets available to create carriers. This can be seen in the higher power curves in Fig. 5.8(b). The curves show that the time required to reach a maximum shortens, and the magnitude increases sub-linearly.

Another set of experimental curves is shown in Fig. 5.8(b), where the excitation wavelength changes from 530 nm to 585 nm. Unlike the previous change of excitation pulse energy, the changes of wavelength have more complicated implications. For a 530 nm excitation, the absorption depth is about 7 μm, whereas for 585 nm it becomes about 118 μm. The different initial exciton distribution due to the difference in absorption constants will create different exciton densities, and the change of photocurrent dynamics is similar to the one in Figure 5.8(a). When the excitation wavelength is shortened, the absorption constant increases, which effectively creates a higher density of excitons. This results in shortening of the photocurrent peak arrival time, which is similar to excitation power increase experiments. This

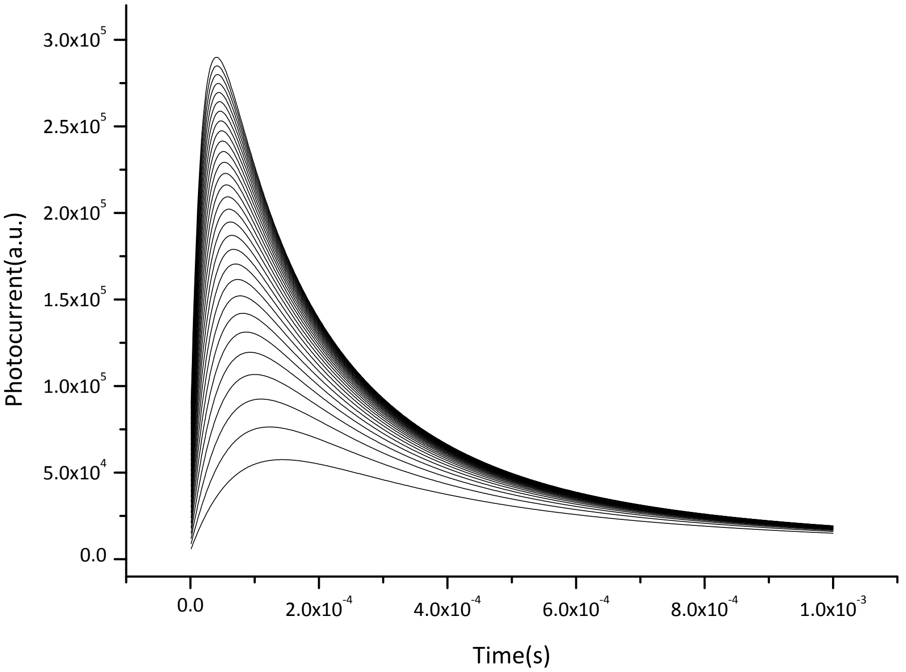

(a) Photocurrent with different initial conditions as shown is Figure 4.2

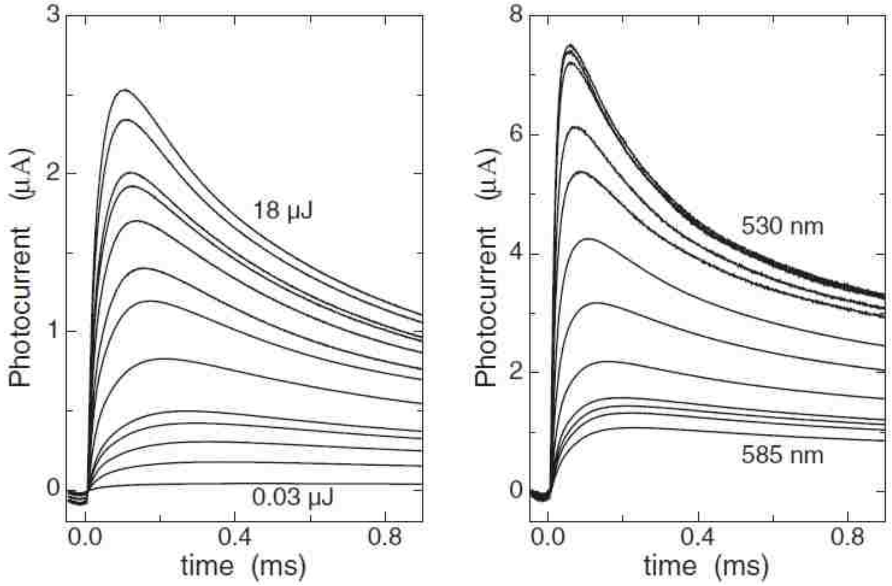

(b) Photocurrent dependence on the excitation at different powers, On the left, 580 nm excitation with increasing excitation energies from 0.03 μJ up to 18 mJ were used. On the right, photocurrent measured with excitation at 530 nm to 585 nm with 5 nm step excited by a pulse energy of 1.4 μJ is shown.

Figure 5.8: Comparison of Power dependent simulation and experimental results of photocurrent

is similar to the data presented in Fig. 2.7, where the total number of excitons was fixed during the excitation-wavelength-dependent experiments. There are still slight differences with the magnitudes observed, but the dynamics agree with our calculations.

5.6 Photocurrent Analysis

Previously in Chapter 4, we have calculated various values from our simulations to understand the photocurrent dynamics. We will focus on the integral of the photocurrent, and the build up time, and compare these values with experimental data.

Analysis of photocurrent experiments are shown in Figure 5.9(c). One can see that when the excitation power (initial singlet population density) increases, a linear relationship for photocurrent integral changes into a sub-linear correlation, as predicted in Figure 5.9(a). In 5.9(c) the buildup time shows to be constant for low densities and to increase quadratically as predicted in the build up time analysis of our model simulations in Figure 5.9(b).

5.7 Conclusion

In this chapter, photoluminescence and photocurrent experimental data were presented and compared with calculations in previous chapters. The photoluminescence have shown to decay quadratically, as the model predicted in Chapter 2. Photocurrent dynamics also agree with the predictions in Chapter 4. In addition, a delayed photocurrent and a shortening of build up time as well as charge carrier lifetime were

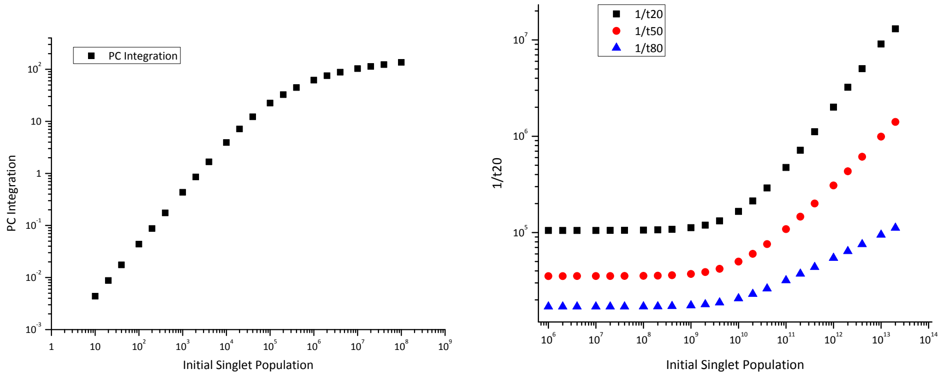

(a) Photocurrent Integral of various initial singlet population densities from Figure 4.3

(b) The Build Up Time for various initial singlet population densities from Figure 4.5

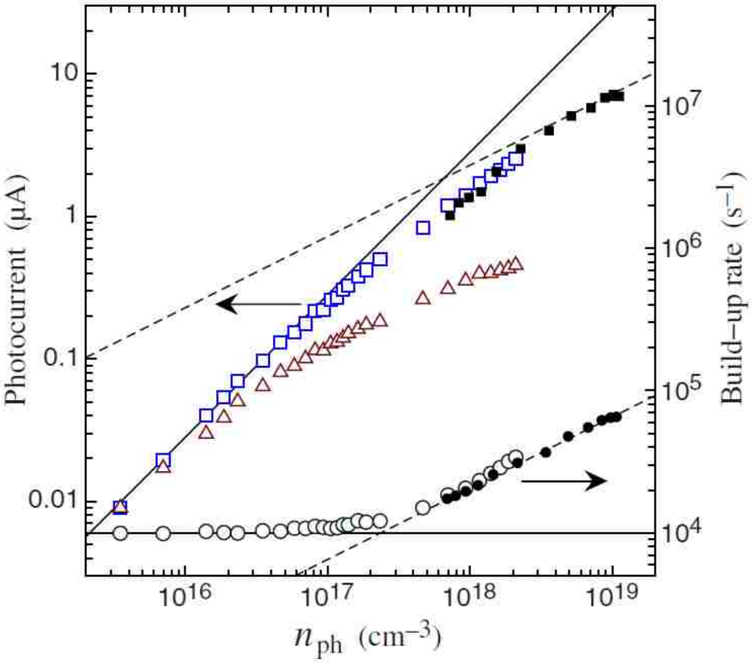

(c) Photocurrent amplitude (open squares), buildup rate (open circles), and photocurrent integral (triangles) v.s the average density of absorbed photons, as determined from the known absorption constant of rubrene and the energy density of the illuminating pulse. Data were collected by varying the laser pulse energy at a fixed wavelength of 580 nm. Solid circles represent additional data points extending to higher photon densities obtained by varying the illumination wavelength at a fixed energy density of 3.5 mJ/cm2. The solid lines represent to the (linear) low-exposure limit, while the dashed lines represent a square-root dependence of the absorbed photon density. From Ref [32]

Figure 5.9: Comparison of calculated photocurrent integral and build up time.

observed as predicted. Additional numerical analysis of photocurrent by calculating the photocurrent integral with the build up time proved to be in agreement with the analysis of the calculated photocurrent in Chapter 4.

Chapter 6

Conclusion

6.1 Conclusions

We have developed and explored a model based on exciton dynamics to explain the unique photoluminescence and photocurrent in rubrene. We have also proposed and a photocurrent model with different variations. The photoluminescence models and photocurrent models support the findings from the photoluminescence and photocurrent experiments.

In summary, with the triplet exciton model and experimental confirmation, we were able to construct a broad picture of what occurs in a rubrene single crystal after impulsive photoexcitation.

After excitation by light, the created excitons are distributed near the surface according to the absorption constant of the wavelength of the excitation light, and its polarization. The photoexcited singlet excitons undergo several processes. First, they radiately decay, which is observed through photoluminescence that decays exponentially with a corresponding lifetime of a few ns. They also create charge carriers, which corresponds with the fast-created photocurrent observed. Finally, they create triplet excitons via fission, which comes into play for effects that occur at long time scales, up to 100 μs in rubrene.

The triplets, due to their forbidden transition, have a relatively long lifetime, which is approximately 100 μs in rubrene single crystals. The triplet excitons have a possibility of interacting with each other to re-create singlet excitons via fusion, and these singlets contribute towards luminescence in the μs regime. This process is dependent on the interaction rate of triplets, which is dependent in turn on its density. Therefore this process only occurs and is observed in high exciton population density regime.

The most profound effect of triplets is that charge carriers can be created with high efficiency near the surface of the rubrene crystal, with the increase of charge carrier population up until about 100 μs. The charge carriers decay with a lifetime of around 6 ms.

6.2 Unknown Processes and Future Experiments

6.2.1 Processes in nanosecond time scale

Although most of the exciton behavior have been understood, some questions still remain. As discussed above, the creation of the fast photocurrent has not been fully understood, let alone its rapid decay. At lower powers, the fast photocurrent increases linearly with the excitation power, indicating a “linear” process. Excitations with a long wavelength (such as 600 nm) also create a fast current component, thus charge carriers are also created by excitons in these conditions. At higher powers there are more complications, where a rapid decay process associated with only this high power regime is observed.

Observations of a gradual exponential increase of photocurrent within a few ns could directly prove that dissociation of singlet excitons to charge carriers exists. However, higher powers [44, 49], creation of charge carriers have been reported to be almost instantaneous.

Some studies have reported [22] that the singlet has a much faster lifetime. In Figure 2.3, one can see that under different initial singlet populations, the singlet lifetime in the first few ns can differ, and the singlets decay can alter between an exponential decay to a quadratic decay. Our model allows different singlets lifetimes, which are determined by its initial population density.

6.2.2 Dissociation of Triplets to Charge Carriers

We have discussed two possible mechanisms of triplets that "linearly" create charge carriers. The role of trap levels is still unknown, or, to be precise, the existence of trap levels or its interaction with excitons is an open question. One reason for considering a trap-assisted charge carrier creation comes from the fact that the carrier creation happens mostly on the surface of the crystal. Previously, a non-homogeneous distribution of the electric field was suspected to be a reason we observed more photocurrent when the exciton population was distributed near the surface (via wavelength-dependent measurements). The electric field calculations show in order to decrease the electric field significantly, a depth of several hundreds of μm is required. However, most of our experiments were executed with an absorption depth of 10 to 100 μm, in which a rather constant electric field existed.

Two models have been proposed: one for when a single triplet interacts with trap levels to create a single hole, and the second for when a triplet occupies a trap level to interact with another triplet to create a electron hole pair. The former model is simple, but might show saturation of photocurrent creation when the initial singlet densities are high, leading to saturation of the trap levels. This was not observed, for at high densities quadratic effects of triplet fusion is dominant, and we observe suppression of photocurrent creation whatsoever. The latter model predicts a quadratic increase in low singlet densities which, we have not observed. If the latter model is true and the quadratic increase existed, it is possible that it was hidden in the limitations of measurements in extreme low densities. Both models are still valid, but lack of observation of any super-linear increase of photocurrent in low densities have put the former model slightly in favor.

In addition, we observed an increase of photocurrent of samples that have been exposed in air for up to a year in an exploratory observation. One can assume oxidized molecules or diffusion of oxygen (or nitrogen, water) into the lattice playing a strong role, which in turn creates trap levels. Various studies already show oxidation being related to increase of photocurrent [34, 44, 50–53].

Bibliography

[1] Podzorov, V., Pudalov, V. & Gershenson, M. Field-effect transistors on rubrene single crystals with parylene gate insulator. *Appl. Phys. Lett.* **82**, 1739 – 41 (2003). URL `http://dx.doi.org/10.1063/1.1560869`.

[2] de Boer, R., Gershenson, M., Morpurgo, A. & Podzorov, V. Organic single-crystal field-effect transistors. *Phys. Status Solidi A* **201**, 1302 – 31 (2004). URL `http://dx.doi.org/10.1002/pssa.200404336`.

[3] Menard, E. *et al.* High-performance n- and p-type single-crystal organic transistors with free-space gate dielectrics. *Adv. Mater.* **16**, 2097–2101 (2004). URL `http://dx.doi.org/10.1002/adma.200401017`.

[4] Sundar, V. C. *et al.* Elastomeric transistor stamps: Reversible probing of charge transport in organic crystals. *Science* **303**, 1644–1646 (2004). URL `http://www.sciencemag.org/content/303/5664/1644.abstract`.

[5] Silinsh, E. & Capek, V. *Organic Molecular Crystals. Interaction, Localization and Transport Phenomena* (American Institute of Physics Press, New York, 1994).

[6] Pope, M. & Swenberg, C. *Electronic Processes in Organic Crystals and Polymers* (Oxford University Press, 1999).

[7] Jurchescu, O. D., Meetsma, A. & Palstra, T. T. M. Low-temperature structure of rubrene single crystals grown by vapor transport. *Acta Crystallographica Section B* **B62**, 330ñ334 (2006).

[8] Laudise, R. A., Kloc, C., Simpkins, P. G. & Siegrist, T. Physical vapor growth of organic semiconductors. *Journal of Crystal Growth* **187**, 449 – 454 (1998). URL `http://www.sciencedirect.com/science/article/pii/S0022024898000347`.

[9] Bayrakceken, F. A new type of delayed fluorescence of rubrene in solution. *Journal of Luminescence* **54**, 29 – 33 (1992). URL `http://www.sciencedirect.com/science/article/pii/002223139290046C`.

[10] Hall, J. L., Jennings, D. A. & McClintock, R. M. Study of anthracene fluorescence excited by the ruby giant-pulse laser. *Phys. Rev. Lett.* **11**, 364–366 (1963).

[11] Birks, J. B., King, T. A. & Munro, I. H. The photoluminescence decay of organic crystals. *Proceedings of the Physical Society* **80**, 355 (1962). URL `http://stacks.iop.org/0370-1328/80/i=2/a=302`.

[12] Kepler, R. G., Caris, J. C., Avakian, P. & Abramson, E. Triplet excitons and delayed fluorescence in anthracene crystals. *Phys. Rev. Lett.* **10**, 400–402 (1963).

[13] M. Pope, F. V., N. E. Geacintov. Singlet exciton fission and triplet-triplet exciton fusion in crystalline tetracene. *Mol. Cryst. Liq. Cryst.* **6**, 83–104 (1969).

[14] Yildiz, A., Kissinger, P. T. & Reilley, C. N. Triplet –¿ triplet fluorescence of rubrene in solution. *The Journal of Chemical Physics* **49**, 1403–1406 (1968). URL `http://link.aip.org/link/?JCP/49/1403/1`.

[15] Jortner, J., Choi, S.-i., Katz, J. L. & Rice, S. A. Triplet energy transfer and triplet-triplet interaction in aromatic crystals. *Phys. Rev. Lett.* **11**, 323–326 (1963).

[16] Tarasov, V. V., Zoriniants, G. E., Shushin, A. I. & Triebel, M. M. The role of spin-lattice relaxation in magnetic field effects on the luminescence of amorphous and polycrystalline rubrene films. *Chemical Physics Letters* **267**, 58 – 64 (1997).

[17] Cai, M. *et al.* Photoluminescence-detected magnetic resonance (pldmr) study of rubrene and oxygen-doped rubrene films and powders. *Proc. SPIE* **7415**, 74151Y (2009).

[18] Zimmerman, P. M., Zhang, Z. & Musgrave, C. B. Singlet fission in pentacene through multi-exciton quantum states. *Nat. Chem.* **2**, 648–652 (2010).

[19] Liu, D. K. K. & Faulkner, L. R. P-type delayed fluorescence from rubrene. *Journal of the American Chemical Society* **99**, 4594–4599 (1977). URL `http://pubs.acs.org/doi/abs/10.1021/ja00456a011`.

[20] Kalinowski, J. *Organic Light Emitting Diodes: Principles, Characteristics, and Processes* (Marcel Dekker, New-York, 1999).

[21] Tao, S. *et al.* Optical pump-probe spectroscopy of photocarriers in rubrene single crystals. *Phys. Rev. B* **83**, 075204 (2011). URL `http://link.aps.org/doi/10.1103/PhysRevB.83.075204`.

[22] Ma, L. *et al.* Singlet fission in rubrene single crystal: direct observation by femtosecond pump-probe spectroscopy. *Phys. Chem. Chem. Phys.* **14**, 8307–8312 (2012).

[23] Ryasnyanskiy, A. & Biaggio, I. Triplet exciton dynamics in rubrene single crystals. *Phys. Rev. B* **84**, 193203 (2011). URL `http://link.aps.org/doi/10.1103/PhysRevB.84.193203`.

[24] Irkhin, P. & Biaggio, I. Direct imaging of anisotropic exciton diffusion and triplet diffusion length in rubrene single crystals. *Phys. Rev. Lett.* **107**, 017402 (2011). URL `http://link.aps.org/doi/10.1103/PhysRevLett.107.017402`.

[25] Tavazzi, S. *et al.* Generalized ellipsometry and dielectric tensor of rubrene single crystals. *Journal of Applied Physics* **102**, 023107 (2007). URL `http://link.aip.org/link/?JAP/102/023107/1`.

[26] Najafov, H., Lyu, B., Biaggio, I. & Podzorov, V. Two mechanisms of exciton dissociation in rubrene single crystals. *Applied Physics Letters* **96**, 183302 (2010). URL `http://link.aip.org/link/?APL/96/183302/1`.

[27] Montemezzani, G., Rogin, P., Zgonik, M. & Günter, P. Interband photorefractive effects: Theory and experiments in knbo$_3$. *Phys. Rev. B* **49**, 2484–2502 (1994). URL `http://link.aps.org/doi/10.1103/PhysRevB.49.2484`.

[28] Snchez-Carrera, R. S. *Theoretical characterization of charge transport in organic molecular crystals*. Ph.D. thesis, Georgia Institute of Technology (2008).

[29] Bisri, S. Z. *et al.* High mobility and luminescent efficiency in organic single-crystal light-emitting transistors. *Advanced Functional Materials* **19**, 1728–1735 (2009). URL `http://dx.doi.org/10.1002/adfm.200900028`.

[30] Hangleiter, A. Nonradiative recombination via deep impurity levels in semiconductors: The excitonic auger mechanism. *Phys. Rev. B* **37**, 2594–2604 (1988). URL `http://link.aps.org/doi/10.1103/PhysRevB.37.2594`.

[31] Chen, C.-H. & Meng, H.-F. Defect auger exciton dissociation and impact ionization in conjugated polymers. *Phys. Rev. B* **64**, 125202 (2001). URL `http://link.aps.org/doi/10.1103/PhysRevB.64.125202`.

[32] Najafov, H., Lyu, B., Biaggio, I. & Podzorov, V. Investigating the origin of the high photoconductivity of rubrene single crystals. *Phys. Rev. B* **77**, 125202 (2008).

[33] Takenobu, T. *et al.* High current density in light-emitting transistors of organic single crystals. *Phys. Rev. Lett.* **100**, 066601 (2008). URL `http://link.aps.org/doi/10.1103/PhysRevLett.100.066601`.

[34] Tsetseris, L. & Pantelides, S. Modification of the electronic properties of rubrene crystals by water and oxygen-related species. *Organic Electronics* **10**, 333 – 340 (2009).

[35] Kloc, C., Tan, K. J., Toh, M. L., Zhang, K. K. & Xu, Y. P. Purity of rubrene single crystals. *Appl. Phys. A.* **95**, 219 (2009).

[36] Weinberg-Wolf, J. R., McNeil, L. E., Liu, S. & Kloc, C. Evidence of low intermolecular coupling in rubrene single crystals by raman scattering. *Journal of Physics: Condensed Matter* **19**, 276204 (2007). URL `http://stacks.iop.org/0953-8984/19/i=27/a=276204`.

[37] Najafov, H., Biaggio, I., Podzorov, V., Calhoun, M. F. & Gershenson, M. E. Primary photoexcitations and the origin of the photocurrent in rubrene single crystals. *Phys. Rev. Lett.* **96**, 056604 (2006). URL `http://link.aps.org/abstract/PRL/v96/e056604`.

[38] Darmanyan, A. P. Nature of lasting luminescence of rubrene in solution. *Russian Chemical Bulletin* **31**, 1679–1682 (1982). URL `http://dx.doi.org/10.1007/BF00956909`. 10.1007/BF00956909.

[39] Matsui, A. Picosecond spectroscopy of exciton relaxation in organic crystals. *J. Opt. Soc. Am. B* **7**, 1615 – 29 (1990). URL `http://www.opticsinfobase.org/abstract.cfm?URI=josab-7-8-1615`.

[40] Sumi, H. Exciton polarons of molecular crystal model. i. —dynamical cpa—. *Journal of the Physical Society of Japan* **36**, 770–779 (1974). URL `http://jpsj.ipap.jp/link?JPSJ/36/770/`.

[41] Cordella, F., Orru, R., Loi, M., Mura, A. & Bongiovanni, G. Transient hot-phonon-to-exciton spectroscopy in organic molecular semiconductors. *Phys. Rev. B* **68**, 113203 – 1 (2003). URL `http://dx.doi.org/10.1103/PhysRevB.68.113203`.

[42] Hegmann, F., Tykwinski, R., Lui, K., Bullock, J. & Anthony, J. Picosecond transient photoconductivity in functionalized pentacene molecular crystals probed by terahertz pulse spectroscopy. *Phys. Rev. Lett.* **89**, 227403 – 1 (2002). URL `http://dx.doi.org/10.1103/PhysRevLett.89.227403`.

[43] Ostroverkhova, O. *et al.* Bandlike transport in pentacene and functionalized pentacene thin films revealed by subpicosecond transient photoconductivity measurements. *Phys. Rev. B* **71**, 35204 – 1 (2005). URL `http://dx.doi.org/10.1103/PhysRevB.71.035204`.

[44] Ostroverkhova, O. *et al.* Ultrafast carrier dynamics in pentacene, functionalized pentacene, tetracene, and rubrene single crystals. *Appl. Phys. Lett.* **88**, 162101 (2006). URL `http://link.aip.org/link/APPLAB/v88/i16/p162101/`.

[45] Jundt, C. *et al.* Exciton dynamics in pentacene thin films studied by pump-probe spectroscopy. *Chem. Phys. Lett. (Netherlands)* **241**, 84 – 8 (1995). URL `http://dx.doi.org/10.1016/0009-2614(95)00603-2`.

[46] Agostini, G., Corvaja, C., Giacometti, G. & Pasimeni, L. Delayed-fluorescence odmr and epr studies of triplet excitons in charge-transfer molecular crystals. *Chemical Physics* **77**, 233241 (1983).

[47] Itoh, K. & Honda, K. Sensitized delayed fluorescence of rubrene. large temperature dependence of triplet lifetime of rubrene. *Chemical Physics Letters* **87**, 213 – 216 (1982).

[48] Kleinerman, M., Azarraga, L. & McGlynn, S. Emissivity and photoconductivity of organic molecular crystals. *J. Chem. Phys.* **37**, 1825–1834 (1962).

[49] Saeki, A., Seki, S., Takenobu, T., Iwasa, Y. & Tagawa, S. Mobility and dynamics of charge carriers in rubrene single crystals studied by flash-photolysis microwave conductivity and optical spectroscopy. *Adv. Mater.* **20**, 920–923 (2008). URL `http://dx.doi.org/10.1002/adma.200702463`.

[50] Maliakal, A. J. *et al.* Mechanism for oxygen-enhanced photoconductivity in rubrene: Electron transfer doping. *Chemistry of Materials* **21**, 5519–5526 (2009). URL `http://pubs.acs.org/doi/abs/10.1021/cm902699s`. `http://pubs.acs.org/doi/pdf/10.1021/cm902699s`.

[51] Mitrofanov, O. *et al.* Oxygen-related band gap state in single crystal rubrene. *Phys. Rev. Lett.* **97**, 166601 (2006). URL `http://link.aps.org/abstract/PRL/v97/e166601`.

[52] Tsetseris, L. & Pantelides, S. T. Large impurity effects in rubrene crystals: First-principles calculations. *Phys. Rev. B* **78**, 115205 (2008).

[53] Najafov, H., Lee, B., Zhou, Q., Feldman, L. C. & Podzorov, V. Observation of long-range exciton diffusion in highly ordered organic semiconductors. *Nat. Mater.* **9**, 938–943 (2010). URL `http://dx.doi.org/10.1038/nmat2872`.

Publications

Articles in peer-reviewed journals

1. "Investigating the origin of the high photoconductivity of rubrene single crystals." Najafov, H., Lyu, B., Biaggio, I., Podzorov, V., *Phys. Rev. B*, **2008**, 77, 125202
2. "Two mechanisms of exciton dissociation in rubrene single crystals." Najafov, H., Lyu, B., Biaggio, I., Podzorov, V., *Applied Physics Letters*, **2010**, 96, 183302

Vita

ByungGook Lyu was born on January 16^{th}, 1978 in Changwon, South Korea. He performed his undergraduate studies in Korea Advanced Institute of Science and Technology between 1995 and 2004. During 1997-1999 he served the Korean navy. He started his graduate studies at Lehigh University in 2005, where he was awarded a Master's degree in Physics in January of 2007, and his PhD in Physics in 2013.